Ocean Acidification trends and Carbonate System dynamics across the North Atlantic Subpolar Gyre water masses during 2009-2019

David Curbelo-Hernández[1], Fiz F. Pérez[2], Melchor González-Dávila[1,*], Sergey V. Gladyshev[3], Aridane G. González[1], David González-Santana[1], Antón Velo[2], Alexey Sokov[3], and J. Magdalena Santana-Casiano[1].

[1] Instituto de Oceanografía y Cambio Global (IOCAG), Universidad de Las Palmas de Gran Canaria (ULPGC). Las Palmas de Gran Canaria, Spain.

[2] Instituto de Investigaciones Marinas (IIM), CSIC, Vigo, Spain.

[3] P. P. Shirshov Institute of Oceanology, Russian Academy of Sciences, Moscow, Russian Federation

*Corresponding Author: Melchor González-Dávila (melchor.gonzalez@ulpgc.es)

Keypoints:

During the 2010s, the subpolar North Atlantic experienced a 50-86% increase in anthropogenic CO_2, accelerating by 7-10% the acidification.

Anthropogenic CO_2 contributed to acidification by 53-68% in upper layers and >82% in the interior ocean.

The acidification trends (0.0006 and 0.0032 units yr^{-1}) declined the Ω_{Ca} and Ω_{Arag} by 0.004-0.021 and 0.003-0.0013 units yr^{-1}, respectively.

Abstract

The CO_2-carbonate system dynamics in the North Atlantic Subpolar Gyre (NASPG) were evaluated between 2009 and 2019. Data was collected aboard eight summer cruises through the CLIVAR 59.5ºN section. The Ocean Acidification (OA) patterns and the reduction in the saturation state of calcite (Ω_{Ca}) and aragonite (Ω_{Arag}) in response to the increasing anthropogenic CO_2 (C_{ant}) were assessed within the Irminger, Iceland and Rockall basins during a poorly-assessed decade in which the physical patterns reversed in comparison with previous well-known periods. The observed cooling, freshening and enhanced ventilation increased the interannual rate of accumulation of C_{ant} in the interior ocean by 50-86% and the OA rates by close to 10%. The OA trends were 0.0013-0.0032 units yr^{-1} in the Irminger and Iceland basin and 0.0006-0.0024 units yr^{-1} in the Rockall Trough, causing a decline in Ω_{Ca} and Ω_{Arag} of 0.004-0.021 and 0.003-0.0013 units yr^{-1}, respectively. The C_{ant}-driven rise in total inorganic carbon (C_T) was the main driver of the OA (contributed by 53-68% in upper layers and >82% toward the interior ocean) and the reduction in Ω_{Ca} and Ω_{Arag} (>64%). The transient decrease in temperature, salinity and A_T collectively counteracts the C_T-driven acidification by 45-85% in the upper layers and in the shallow Rockall Trough and by <10% in the interior ocean. The present investigation reports the acceleration of the OA within the NASPG and expands knowledge about the future state of the ocean.

Keywords: Ocean Acidification, Anthropogenic Carbon, North Atlantic Subpolar Gyre.

1. Introduction

The ocean uptake of approximately one-third of the CO_2 released into the atmosphere (Friedlingstein et al., 2023; Gruber et al., 2019a) has an important role in the climate regulation causing changes in the marine carbonate chemistry. The exponential increase in the global ocean CO_2 sink in phase with those of anthropogenic emissions (Friedlingstein et al., 2023) has resulted in a long-term decrease in the concentration of carbonate ions ($[CO_3^{2-}]$) and pH. This process has been collectively referred to as Ocean Acidification (OA; Caldeira and Wickett, 2005, 2003; Doney et al., 2009; Orr et al., 2005; Raven et al., 2005; Feely et al., 2009) and favour the dissolution of calcium carbonate ($CaCO_3$). It affects not only calcifying marine organisms and ecosystems which use the biogenic $CaCO_3$ forms of calcite and aragonite (e. g. Gattuso et al., 2015; Langdon et al., 2000; Pörtner et al., 2004, 2019; Riebesell et al., 2000) but also the global biogeochemical cycles (Gehlen et al., 2011; Matear and Lenton, 2014).

The absorption of anthropogenic CO_2 has reduced the pH of the global surface ocean by 0.1 units since preindustrial times, representing approximately a 30% increase in acidity (Caldeira and Wickett, 2003). According to the IPCC's Representative Concentration Pathways (RCPs) scenarios (Van Vuuren et al., 2011; Moss et al., 2010), which project various future trajectories of greenhouse gas concentrations, the model projections estimate a potential pH decrease of 0.3–0.4 units by the end of the century under the RCP8.5 scenario, which assumes continued high CO_2 emissions. In contrast, the most conservative RCP2.6 scenario, which includes significant emission reductions, anticipates a pH drop of 0.2–0.3 units (IPCC 2013 and 2021). However, as the absorption and storing of anthropogenic carbon (C_{ant}), defined as the fraction of inorganic carbon resulted from human emissions (Sarmiento et al., 1992), is not uniform within the ocean (Sabine et al., 2004a), OA rates may show a significant spatial variability and should be regionally studied. The temporal evolution of the carbonate system variables in surface waters are monitored and assessed in several time-series stations located across different ocean regions (Bates et al., 2014). The largest OA rates are expected to occur across high northern and southern latitudes (Bellerby et al., 2005; Orr et al., 2005), where deep convective overturning and subduction occur favouring the entrance of C_{ant} in the interior ocean (Maier-Reimer and Hasselmann, 1987; Lazier et al., 2002; Sarmiento et al., 1992).

The North Atlantic is one of the strongest CO_2 sinks and stores over 25% of the C_{ant} accumulated in the global ocean (e. g. Gruber et al., 2019; Khatiwala et al., 2013; Pérez et al., 2024, 2010, 2008, 2024; Sabine et al., 2004; Takahashi et al., 2009). The Atlantic Meridional Overturning Circulation (AMOC) plays a significant role by conveying acidified C_{ant}-loaded waters polewards and exporting them to the ocean interior across deep-water formation areas (Lazier et al., 2002; Pérez et al., 2013, 2008; Steinfeldt et al., 2009). It contributes to homogenize the C_{ant} and pH in the whole water column in such regions and exported these properties southwards to the global deep ocean (Perez et al., 2018). Thus, the North Atlantic behaves as a crucial region for understanding the impacts of anthropogenic forcing on the global ocean.

OA has been widely studied in the North Atlantic through the monitoring of the ocean physicochemical properties at time-series stations (summarized by Bates et al., 2014) placed in subtropical and subpolar latitudes: the European Station for Time series in the Ocean at the Canary Islands (ESTOC; 29.04ºN, 15.50ºW; González-Dávila et al., 2010; González-Dávila and Santana-Casiano, 2023; Santana-Casiano et al., 2007), the Bermuda Atlantic Time-series Study (BATS; 32.0ºN, 64.0ºW; Bates et al., 2012), the Irminger Sea Time Series (IRM-TS; 64.3ºN, 28.0ºW; Olafsson et al., 2010) and the Iceland Sea Time Series (IS-TS; 68.0ºN, 12.66ºW; Olafsson et al., 2009, 2010). OA rates has also been evaluated along transects through repeated hydrographic cruises (i.e. Guallart et al., 2015; García-Ibáñez et al., 2016; Vázquez-Rodríguez et al., 2012b) or even covered by volunteer observing ships (Fröb et al., 2019). These investigations have revealed a rate of decrease in pH of ~0.001-0.002 units yr^{-1}. Moreover, González-Dávila and Santana-Casiano (2023) has recently indicated that these rates are increasing since 1995.

The assessment of OA is of especial interest across the North Atlantic Subpolar Gyre (NASPG; 50-60ºN), where the atmospheric CO_2 sink is particularly strong and the deep-water formation processes favour the storage of C_{ant} through the whole water column (Gruber et al., 2019b; Sabine et al., 2004b; Watson et al., 2009, Pérez et al. 2008). Likewise, the deep-water formation processes create the largest and deepest ocean environments supersaturated for aragonite (at more than 2000 m depth; Feely et al., 2004; Jiang et al., 2015), which is the main $CaCO_3$ mineral for Cold-water corals (CWC; Roberts et al., 2009) and some pteropods

(Bathmann et al., 1991; Urban-Rich et al., 2001). These deep biomes are predicted to be one of the first in the global ocean affected by OA, mainly due to the shoaling of the Aragonite Saturation Horizon and its progressive exposition to undersaturated conditions for aragonite at intermediate and deep waters (Gehlen et al 2014; Guinotte et al., 2006; Raven et al., 2005; Roberts et al., 2009; Turley et al., 2007).

The physical processes along the NASPG, which are subject to significant spatiotemporal variability introduced by the atmospheric forcing and climatology on an interannual scale, directly influenced the biogeochemistry (Corbière et al., 2007; Fröb et al., 2019). The changes in North Atlantic Current (NAC) modifies the poleward heat transport from subtropical latitudes and the air-sea interactions, influencing temperature patterns (Josey et al., 2018; Mercier et al., 2015). Recent studies noticed the surface cooling and freshening of the NASPG in the 2010s (Holliday et al., 2020; Josey et al., 2018; Robson et al., 2016; Tesdal et al., 2018) contrasting with the period of warming and salinification in the 1990s extended until 2005 (Häkkinen and Rhines, 2004; Hátún et al., 2005; Robson et al., 2014). Anomalously heat loss and winter deep convection were found to be of high intense since 2008 contributing to the extreme cold anomaly along the NASPG (e. g. De Jong et al., 2012; de Jong and de Steur, 2016; Fröb et al., 2019, 2016; Gladyshev et al., 2016b, 2016a; Piron et al., 2017; Våge et al., 2009). These fluctuations in the vertical mixing and ocean circulation patterns introduces changes in the distribution of the carbonate system variables.

The estimated OA trend over 1991-2011 for surface waters across the North Atlantic Subpolar biome was -0.0020 ± 0.0001 units yr^{-1} (Lauvset et al., 2015). Chau et al., 2024 recently reported that the surface waters in the Irminger and Iceland basins has acidified over 1985-2021 at rates of -0.0016 ± 0.0001 and -0.0014 ± 0.0001 units yr^{-1}. Several observation-based investigations have evaluated the drivers, trends and impacts of OA through the entire water column in the Irminger and Iceland basins (e. g. Fontela et al., 2020; García-Ibáñez et al., 2021, 2016; Perez et al., 2018; Pérez et al., 2021; Ríos et al., 2015), while few studies have addressed it in the Rockall Trough (e. g. McGrath et al., 2013, 2012a, 2012b, Humphreys et al., 2016) due to lack of repeated hydrographic sections or time-series stations and subsequent limitation of continuous surface-to-bottom data. The high longitudinal variability in the NASPG caused by the influence of different circulation patterns and water masses (García-Ibáñez et al., 2018,

2015) introduced several physicochemical heterogeneities between the Irminger and Iceland with the Rockall basin (Ellett et al., 1986; McGrath et al., 2013, 2012b; Holliday et al., 2000). These differences in the distributions of Marine Carbonate System (MCS) variables should be considered to improve our understanding of OA in the entire North Atlantic.

This study evaluated the OA in the NASPG across the Irminger, Iceland and Rockall basins during the 2010s. High-quality direct measurements of CO_2 system variables from eight hydrographic cruises occupying 59.5ºN between 2009 and 2019 were used to evaluate the drivers and trends of pH, and the potential effects of OA on calcifying organisms of changes in calcite (Ω̆Ca) and aragonite (Ω̆Ar) saturation states. This study advances our understanding of the complexities associated with OA in the NASPG and supports ongoing efforts to model and predict future acidification scenarios in the North Atlantic and global ocean.

2. Methodology

2.1. Data collection

Data were collected from eight summer cruises conducted along the transverse hydrographic section at 59.5ºN between 2009 and 2019 (Daniault et al., 2016; Gladyshev et al., 2016b, 2017, 2018; Sarafanov et al., 2018). This section is part of the World Climate Research Programme (WCRP) within the framework of the CLIVAR (Climate and Ocean: Variability, Predictability and Change) project and covers the length of the Subpolar North Atlantic between Scotland and Greenland (4.5-43.0ºW), crossing the Irminger and Iceland basins and the Rockall Trough (Figure 1). Generally, the sampling stations were equidistantly spaced every 20 nmi apart (~1/3º longitude) and repeated in all the cruises except for the cruise of 2016, when the station spacing was decreased to 10 nmi over Reykjanes Ridge western and eastern slopes. The distance between stations over the east Greenland slope and shelf always decreased from 10 nmi to about 2 nmi. The surface-to-bottom sampling and in situ measurements were performed by using a SBE 911plus CTD with SBE32 Carousel containing 24 Niskin bottles (10 L) with additional sensors for pressure (P), dual temperature (T) and salinity (S), and dissolved oxygen (DO). The eight cruises included in the new dataset are the result of an international collaboration between researchers from the P. P. Shirshov Institute of Oceanology at the Russian Academy of Science and the Marine Chemistry research group from the

Oceanography and Global Change Institute (QUIMA-IOCAG) at the University of Las Palmas de Gran Canaria (ULPGC). A detailed overview of the cruises is given in Table 1.

2.1.1. CO_2 system variables measurements

The analysis of the MCS variables followed the same analytical methodology and provided high-quality CO_2 measurements in all the hydrographic cruises. It includes the sampling and data collection techniques, quality control and calculation procedures published in the updated version of the DOE method manual for CO_2 analysis in seawater given by Dickson et al., 2007. The seawater samples were onboard analysed for total alkalinity (A_T) and total inorganic carbon (C_T) determination by using a VINDTA 3C and following Mintrop et al., (2000). The A_T was analysed by potentiometric titration with HCl to the carbonic acid endpoint and determined through the developing of the full titration curve (Millero et al., 1993; Dickson and Goyet, 1994). The C_T was determined through coulometric titration (Johnson et al., 1993). The VINDTA 3C was calibrated through the titration of Certified Reference Material (CRMs; provided by A. Dickson at Scripps Institution of Oceanography), giving values with an accuracy of ±1.5 µmol kg^{-1} for A_T and ±1.0 µmol kg^{-1} for C_T.

Spectrophotometric pH measurements (Clayton and Byrne, 1993) in total scale at constant temperature of 15ºC ($pH_{T,15}$) were performed for the cruises between 2009 and 2016. A spectrophotometric pH sensor (SP101-SM) developed by the QUIMA-IOCAG group at the ULPGC in collaboration with SensorLab (González-Dávila, 2014; González-Dávila et al., 2016) was used. The method uses 4 wavelengths analysis for pH indicator dyes (m-cresol purple), includes auto-cleaning steps and performs a blank for pH calculation immediately after the dye injection. The spectrophotometric sensor was *in situ* tested by using a TRIS seawater buffer (Ramette et al., 1977) and provided pH_{T15} values with an accuracy of ±0.002 units. To account for the systematic uncertainty reported by DelValls and Dickson (1998) related to the pK* values of m-cresol purple, and in line with their recommendations, a correction of +0.0047 units was applied to the measured pH_{T15}. This adjustment ensures that the calculated pH values are consistent with the more accurate pK* determinations.

2.1.2. Dissolved oxygen (DO) measurements

The WINKLER method introduced by Winkler (1888) and optimized by Carpenter (1965) and Carrit and Carpenter (1966) was used to analytically determine the dissolved oxygen (DO) of the seawater samples in all the cruises from 2009 to 2016. The seawater samples for DO determination were collected from the bottle samples in pre-calibrated glass wide-neck bottles avoiding bubble formation. The temperature of the water was recorded during the sampling. All the reagents and solutions used for dissolved oxygen determination were prepared following the procedures described by Dickson, (1995) and their possible impurities were controlled by determining a blank every 2 days.

As DO could not be analytically measured during the cruise of 2019 (due to limitations related with the oceanographic cruise plan), it was computed for this year by comparing the performance of the DO sensor during the cruise of 2019 versus (1) DO data estimated by a neural network for the cruises of 2016 and 2019 and (2) WINKLER-measured DO data in the cruise of 2016. The neural network ESPER_NN (Empirical Seawater Property Estimation Routine) introduced by Carter et al., (2021) was used for DO estimations. The computational procedure is detailed in Appendix A.

2.2. Data processing

2.2.1. Evaluation of the internal consistency of the data using CANYON-B

The measured and determined data were compared with estimations given by the Bayesian neural network "CANYON-B" (Bittig et al., 2018), a re-developed and more robust neural network based on CANYON (CArbonate system and Nutrients concentration from hYdrological properties and Oxygen using a Neural-network; Sauzède et al., 2017). CANYON-B estimates the four MCS variables (A_T, C_T, pH and pCO$_2$) and macronutrients concentrations (PO_4^{3-}, NO_3^- and Si(OH)$_4$, hereinafter PO$_4$, NO$_3$ and Si(OH)$_4$) as a function of a simple set of input variables which include P, T, S, DO, latitude, longitude and date. This neural network is trained on and validated against bottle data from GLODAPv2 and recent GO-SHIP profiles and compared with sensor data from Argo floats. The standard errors of estimate reported for CANYON-B by Bittig et al., (2018) are 6.3 µmol kg^{-1} for A_T, 7.1 µmol kg^{-1} for C_T, 0.013 units for pH, 20 µatm for pCO$_2$, 0.051 µmol kg^{-1} for PO$_4$, 0.68 µmol kg^{-1} for NO$_3$ and 2.3 µmol kg^{-1} for Si(OH)$_4$. The crossover analysis between measured and estimated data did not show systematic differences but individual outliers. The measured data that were higher/lower than the CANYON-B estimate by plus/minus twice the predicted variable uncertainty of the neural network was considered as outliers and removed from the dataset.

The total amount of measured data was 8974 for A_T, 7495 for C_T, 8706 for $pH_{T,15}$, 9656 for DO, 9114 for PO_4 and 9192 for $Si(OH)_4$. The difference between the measured and CANYON-B-estimated variables (referred hereinafter as canyon-estimated variables) were performed for each sample in which CANYON-B could be applied (samples with availability of T, S and DO measurements). The number of data, mean values and standard deviation of the measured variables for each cruise were summarized in Table S1. The average differences with the 95% confidence interval for each cruise are shown in Table S2. The average differences for the entire period (2009-2019) were lower than 2.1 µmol kg^{-1} for A_T, 2 µmol kg^{-1} for C_T, 0.0002 for pH, 0.02 µmol kg^{-1} for PO_4 and 0.25 µmol kg^{-1} for $Si(OH)_4$. The minimal difference between the measured and canyon-estimated pH infers confidence in the correction applied to the measured pH following DelValls and Dickson (1998).

2.2.2. Computational methods

The computational procedures to calculate MCS system variables applied in this investigation used the $CO_{2,SYS}$ programme developed by Lewis and Wallace, (1998) and run with the MATLAB software (van Heuven et al., 2011; Orr et al., 2018; Sharp et al., 2023). The set of constants used for computations includes the carbonic acid dissociation constants of Lueker et al., (2000), the HSO_4^- dissociation constant of Dickson, (1990), the HF dissociation constant of Perez and Fraga, (1987) and the value of $[B]_T$ determined by Lee et al., (2010). The pH in total scale at *in situ* temperature (pH_T) was computed from the measured A_T and $pH_{T,15}$ (the computed C_T was given as an output). The pH_T for the cruise of 2019, in which direct pH measurements were not performed, was computed from the measured A_T and C_T.

The saturation states of Calcite (Ω_{Ca}) and Aragonite (Ω_{Arag}), determined from the product of the ion concentrations of calcium ($[Ca^{2+}]$) and carbonate ($[CO_3^{2-}]$) divided by the stoichiometry solubility products (K_{sp}) for calcite (K_{Ca}) and aragonite (K_{Arag}) given by Mucci (1983), were generated as outputs of the $CO_{2,SYS}$ computational routine. The decrease in Ω_{Ca} and Ω_{Arag} reports the adverse impacts of OA on marine calcification processes (e. g. Gattuso et al., 2015; Langdon et al., 2000; Pörtner et al., 2004, 2019; Riebesell et al., 2000).

An internal consistency test was conducted on the three measured MCS variables. The measured variables were compared with canyon-estimated and CO_{2SYS}-computed variables. The average differences and standard deviations were summarized in Table S2 and ensure the consistency of the observations. In addition, due to gaps in data, an intercomparison between measured and computed C_T and pH_{T15} was performed. It considers the availability of measurements for each latitude, longitude and time and the differences between the measured and computed pH with the canyon-estimated pH_T. The use of measured or computed C_T followed these conditions: (1) If there is measured C_T but not measured pH, measured C_T was used, (2) if there is measured pH but not measured C_T, computed C_T was used, (3) and if there is measured C_T and pH, measured C_T was used when the differences between measured and canyon pH_T is lower than the differences between computed and canyon-estimated pH_T, while computed C_T was used when the opposite happens. In total, 6375 measured and 2872 computed C_T data were used in this study (69% and 31%, respectively). The average differences in each cruise between the combined (measured and computed, also referred as "$C_{T\,(new)}$") and canyon-estimated C_T variable is provided in Table S2. The amount and percentage of measured and computed C_T data per cruise is given in Table S3. As the measured C_T was in average 1.9 µmol kg^{-1} higher than the canyon-estimated and the computed C_T was in average 1.7 µmol kg^{-1} lower, the new compilation based on these previous conditions allowed to reduce the difference to 1.5 µmol kg^{-1}.

2.2.3. Anthropogenic CO_2 (C_{ant}) calculation

The anthropogenic CO_2 (C_{ant}) was estimated by using the biogeochemical back-calculation ϕC_T^o method, which has an overall estimated uncertainty of ±5.2 µmol kg^{-1} (Pérez et al., 2008; Vázquez-Rodríguez et al., 2009). The method considers the change of C_T between the preindustrial era (1750) and the time of the observations, as well as the processes involved in the uptake and distribution of C_{ant} (biogeochemistry, mixing processes and air-sea fluxes). The C_{ant} was calculated (Eq. 1) as the difference between the C_T at the time of observation, the C_T that the seawater would have in equilibrium with a preindustrial atmosphere (preformed C_T; C_T^{pre}), the offsets of such equilibrium values (air-sea CO_2 disequilibrium; ΔC_T^{dis}) and the changes in C_T due to the organic and carbonate pumps (ΔC_T^{bio}). The C_T and A_T at the time of observations and the preformed A_T (A_T^0) are needed as input parameters and the computational procedure was described by Vázquez-Rodríguez et al., (2012).

$$C_{ant} = C_T - C_T^{pre} - \Delta C_T^{dis} - \Delta C_T^{bio} \quad (1)$$

The ϕC_T^o method is an improved process-based C_{ant} estimation method tested and widely applied in the Atlantic Ocean (Vázquez-Rodríguez et al., 2009) which present distinctive characteristics relative to existing C_{ant} approaches, such as the classical ΔC^* (GSS' 96; Gruber et al., 1996) and the TrOCA (Touratier et al., 2007). The main advantages of the ϕC_T^o method has been described by Pérez et al., (2008).

2.2.4. Hydrographic characterization

The characterization of the basins and water masses was done by considering the 2009-2019 mean combined 59.5ºN section constructed with potential vorticity, dissolved oxygen and salinity together with the large-scale circulation in the North Atlantic (e. g. Lherminier et al., 2010; Pérez et al., 2021; Sarafanov et al., 2012; Schmitz and McCartney, 1993; Schott and Brandt, 2007; Sutherland and Pickart, 2008). A schematic diagram with the main surface and deep currents in the NASPG is depicted in Figure 1a. The basin division considered the NAC pathways and revealed a west-to-east distribution comprising the Irminger and Iceland basins and the Rockall Trough. The Iceland basin was delimited along its eastern boundary by the central NAC branches around the northern part of the Haton Bank and George Bligh Bank, and along its western boundary by the Return Current over the eastern flank of the Reykjanes Ridge slope. This suggest that the Iceland basin could be longitudinally separated in two subregions: the western Iceland basin (24.0-29.5ºW) and the eastern Iceland basin (14.0-24.0ºW).

The upper layers were mainly occupied by Subpolar Mode Waters (SPMW) and North Atlantic Central Waters (NACW). SPMW is formed in the Iceland basin (McCartney and Talley, 1982; Brambilla and Talley, 2008; Tsuchiya et al., 1992; Van Aken and Becker, 1996), flow eastward to the Rockall Trough and recirculate across the Reykjanes Ridge (Brambilla and Talley, 2008). In the Irminger basin, SPMW flow with the Irminger Current to the north over the western Reykjanes Ridge flank and to the south over the eastern Greenland slope (Figure 1a). Thus, SPMW signal was detected in the western and eastern Irminger basin up to 400-700 m depth and limited to subsurface depths in the central part of the basin. NACW were placed above SPMW east of the Irminger basin and separated in two branches: Eastern North Atlantic Central Water (ENACW), formed by winter convection in the intergyre region and moved poleward from the Bay of Biscay through the Rockall Trough (Harvey, 1982; Pollard et al., 1996), and Western North Atlantic Central Water (WNACW), flowing northward with the NAC along the western Iceland basin. The intermediate layers were mainly occupied by Labrador Sea Water (LSW), formed in the Labrador Sea and transported eastward (e. g. Pickart et al., 2003; Fröb et al., 2016). LSW path diverges into two cores when it reaches the Reykjanes Ridge (Álvarez et al., 2004; Pickart et al., 2003): a fraction of LSW rapidly moved to the Irminger basin and incorporated into the Deep Western Boundary Current (DWBC) (Bersch et al., 2007) and a second LSW core was transported eastward into the Iceland and Rockall basins. In the Irminger and western Iceland basin, LSW placed above Iceland-Scotland Overflow Water (ISOW), which originated from the overflow of Norwegian Sea waters over the Iceland–Scotland ridges and flowed southward and below 1500 m depth through the western NASPG (van Aken and de Boer, 1995; Dickson et al., 2002; Fogelqvist et al., 2003). The bottom of the western Irminger basin was occupied by Denmark Strait Overflow Water (DSOW), recently formed from deep waters from the Nordic seas flowing southward over the Greenland-Iceland ridge and sinking through the eastern Greenland slope (Read, 2000; Stramma et al., 2004; Yashayaev and Dickson, 2008). LSW core transported eastwards rises in depth through the western Haton Bank flank and occupy the bottom depths in the eastern Iceland basin and in the Rockall Trough. A low-ventilated thermocline layer is placed between SPMW and LSW in the eastern NASPG (García-Ibáñez et al., 2016), which represent the product of mixing with waters coming from the south (i. e. Mediterranean Waters; MW).

To enhance the comprehension of the spatial distribution and trends of the biogeochemical variables and to facilitate comparisons with previous studies along the NASPG, the hydrographic characterization was simplified based on the following principles: (1) the Iceland basin was not divided into its western and eastern parts and its longitudinal span was delimited by the Reykjanes Ridge (29.5ºW) and the Haton Bank (17ºW), (2) upper Labrador Sea Water (uLSW) was separated from deeper LSW (e. g. Stramma et al., 2004), (3) the weak and spatially-limited influence of the return current and WNACW was removed by considering the upper and intermediate layers of both the Irminger and Iceland basin fully occupied by SPMW above uLSW, and (4) only the east branch of NACW (ENACW), placed above SPMW, was contemplated for the upper Rockall Trough.

The whole water column was separated in layers delimited by potential density isopycnals at a reference pressure of 0 dbar following Azetsu-Scott et al. (2003), Kieke et al. (2007), Pérez et al. (2008) and Yashayaev et al. (2008). The vertically distributed water masses separated in density layers is represented for the entire section in Figure 1b. The vertical characterization in density layers allows to consistently compare the low-variable physical and chemical properties within each water mass, enabling to assume linearity in the ocean CO_2 system. The determination of the isopycnal limits between layers in the Irminger and Iceland basins followed previous biogeochemical studies in the western boundary of the North Atlantic (Fontela et al., 2020; García-Ibáñez et al., 2016; Pérez et al., 2010, 2008; Vázquez-Rodríguez et al., 2012a). The surface-to-bottom distribution of the main water masses in these basins (with their respective σ_0 lower limits shown in brackets) was SPMW (27.68 kg m^{-3}), uLSW (27.76 kg m^{-3}), LSW (27.81 kg m^{-3}) and ISOW (27.88 kg m^{-3}). The low temperature and salinity DSOW were considered at the bottom of the westernmost part of the Irminger basin. The hydrography of the Rockall Trough has been characterized in previous studies in the Northeast Atlantic (e. g. Ellett et al., 1986; Harvey, 1982; McGrath et al., 2012a, 2012b; Holliday et al., 2000), with the main water masses surface-to-bottom distributed as ENACW (27.35 kg m^{-3}), SPMW (27.68 kg m^{-3}) and LSW (bottom).

2.2.5. Data adjustment for trends computation

The interannual trends were analysed through the whole water column across the Irminger, Iceland and Rockall basins by yearly averaging the variables for each layer, following previous studies in the NASPG (e.g. Fontela et al., 2020; García-Ibáñez et al., 2016). Linear regressions were applied to the mean values, in which the value of the slope give the ratios of interannual changes. The errors of the means were calculated through the relation of the Standard Deviation and the square root of the number of bottle samples in each layer and cruise ($Standard\ Deviation/\sqrt{n}$). The standard errors of the slopes were calculated by accounting for the error propagation of the annual mean values. The Pearson correlation test was employed to assess the strength and direction of the linear regressions and evaluate the significance of the interannual trends. This test provided correlation coefficients (r^2) and corresponding p-values to determine statistical significance. The p-values ≤ 0.01 indicated that the trends were statistically significant at the 99% confidence level, the p-values ≤ 0.05 indicated that the trends were statistically significant at the 95% confidence level and the p-values ≤ 0.1 indicated that the trends were statistically significant at the 90% level. Trends with p-values > 0.1 were considered as not statistically significant but provided an estimation of the temporal evolution of the variables in their respective layers. These not statistically significant trends were explained by the high variability and changes in the low-limit depth of the layers encountered between consecutive years.

As there was a lack of in situ measurements and sampling along the west half of the Irminger basin (36.5-42.5ºW) in the cruise of 2019 (due to permit restrictions to study the national waters of Denmark), the GO-SHIP A25-OVIDE data for the cruise of 2018 (available at SEANOE [https://www.seanoe.org/], Lherminier et al., 2022) were considered to adjust the 2019 data. The average values were calculated with both the available data in the easternmost part of the Irminger basin during the cruise of 2019 and the A25-OVIDE-2018 data available in the same part of the section (29.6-36.5ºW). The difference between these average values provides the variation of each variable from 2018 to 2019, which can be extrapolated to the western part of the Irminger basin by assuming linearity in the temporal evolution. Thus, the average values for 2019 were adjusted by applying the product with the calculated change between 2018 and 2019.

2.2.6. Deconvolution of the trends

OA trends arise due to the combined variations in T, S, C_T and A_T. The influence of each driver on OA and subsequent impacts on marine calcification processes was analysed by assuming linearity and employing a first-order Taylor-series deconvolution (Sarmiento and Gruber, 2006) to evaluate the trends for pH_T (Fröb et al., 2019; García-Ibáñez et al., 2016; Pérez et al., 2021; Takahashi et al., 1993; Tjiputra et al., 2014) and Ω (García-Ibáñez et al., 2021). The interannual rates of change of pH_T and Ω result from the sum of their partial derivatives versus T, S, C_T and A_T, calculated based on mean properties of each layer. The most recent equation defined by Pérez et al., (2021) was used (Eq. 2), in which X represents pH_T, Ω_{Ca} and Ω_{Arag}. and salinity-normalized C_T and A_T (NC_T and NA_T, normalized to a constant salinity of 35) were used to remove the effect of the freshwater fluxes and evaporation/precipitation effects.

$$\frac{dX}{dt} = \frac{\partial X}{\partial T}\frac{dT}{dt} + \left(\frac{\partial X}{\partial S} + \frac{NC_T}{S_0}\frac{\partial X}{\partial C_T} + \frac{NA_T}{S_0}\frac{\partial X}{\partial A_T}\right)\frac{dS}{dt} + \frac{S}{S_0}\frac{\partial X}{\partial C_T}\frac{dNC_T}{dt} + \frac{S}{S_0}\frac{\partial X}{\partial A_T}\frac{dNA_T}{dt} \quad (2)$$

It is important to remark that the changes in NA_T and NC_T are linked with biogeochemical processes which have different influences: the processes involved in the organic carbon pump contribute to strongly change the NC_T weakly affecting the NA_T, while those involved in the carbonate pump affect the NA_T twice as much as NC_T. The complexity and heterogeneity of the processes that govern the pH_T change were considered by this equation.

3. Results

The vertical distribution of the physical and biogeochemical variables is depicted for the cruises of 2009 and 2016 in Figures 2, 3, S2 and S3. The subsurface layers were characterized by warmer and saltier waters than intermediate and deep layers among the three basins (Figure 2a and 2b). A West-to-East increase in temperature and salinity throughout the water column was observed in all the cruises. The temperature and salinity signals were highest in the Rockall Trough (4.5-11.0ºC and 35.0-35.4, respectively), followed by the Iceland basin (3.0-7.5ºC and 34.9-35.2, respectively) and the Irminger basin (1.5-6.5ºC and 34.8-35.1, respectively). The longitudinal differences in temperature were more remarkable toward the upper layers through the SPMW and uLSW.

The spatial variability in the physical properties introduced heterogeneities in the distribution of the CO_2 system variables. The A_T show a well-correlated linear relationship with salinity throughout the region (A_T = 54.57 (±0.36) Salinity + 396.7 (± 12.7); r^2=0.90 and p-value < 0.01; Standard Error of Estimate of 2.9 µmol kg^{-1}), with lower and vertically-homogenized average values in the Irminger basin (2302.8-2307.3 µmol kg^{-1} in subsurface waters and 2298.8-2301.0 µmol kg^{-1} in bottom waters) and Iceland basin (2308.7-2315.0 µmol kg^{-1} in subsurface waters and 2305.2-2308.0 µmol kg^{-1} in bottom waters) compared to the Rockall Trough (2317.9-2329.1 µmol kg^{-1} in subsurface waters and 2308.5-2310.9 µmol kg^{-1} in bottom waters).

The upper layers were characterized by low C_T values (2153.7-2160.8 µmol kg^{-1} at the Irminger basin, 2158.1-2168.4 µmol kg^{-1} at the Iceland basin and 2120.1-2131.0 µmol kg^{-1} at the Rockall Trough), while a rapidly increment with depth was found below 100-200 m depth (2154.7-2171.2 µmol kg^{-1} throughout the section). The notable difference in the distribution of

A_T and C_T (Figure 2c and 3a, respectively) compared to those of NA_T and NC_T (Figure S2) elucidated the remarkable significance of freshwater fluxes on the carbon variables fluctuations during the period of study. The entrance of C_{ant} through the atmosphere-seawater interface caused higher C_{ant} values in the upper layers (higher than 50 μmol kg^{-1} in the first 1000 m depth; Figure 3b). The natural component of the C_T (C_{nat}=C_T-C_{ant}; Figure 3c) correlated with C_T (r^2=0.87), and show a distribution characterized by low surface (<2110 μmol kg^{-1}) and high bottom concentrations (>2130 μmol kg^{-1}).

The pH_T (Figure 2d) rapidly decreased with depth showing the effect of biological uptake in the upper layers and remineralization in deeper areas. The subsurface layer up to 100-200 m depth exhibited pH_T values higher than 8.025 units, which fell to 7.975 units at the bottom layers. The pH_T profiles reported an intrusion of remineralized and poorly oxygenated water between 500 and 1000 m depth with relatively low pH_T (<7.975) compared to adjacent layers in the Iceland basin and in the western part of the Rockall Trough. This thermocline layer was previously observed at ~500 m depth by García-Ibáñez et al., (2016) along a more meridional transect which crossed the Iceland basin northwest-southeast. It introduces differences in the intermediate water masses between the Iceland and Rockall basins with the Irminger basin.

The spatial and interannual fluctuations in the ventilation rates through changes in the water mass formation and respiration processes represent a source of variability in the biogeochemical patterns. The apparent oxygen utilization (AOU), defined as the difference between saturated oxygen (calculated following Benson and Krause, 1984) and measured oxygen, was used to assess the ventilation of the water masses (Figure 2e). The high AOU values indicate low ventilation, while low AOU values indicate the opposite. The slow renewal of waters with high AOU favour the accumulation of the product of remineralization (de la Paz et al. 2017). Thus, the areas with higher AOU (Figure 2e) were found to have high concentration of C_T and low pH_T (Figures 3a and 2d, respectively). The near surface waters permanently in contact with the atmosphere exhibited the lowest AOU values (<20 μmol kg^{-1}). The Irminger Basin presents the most significant water column ventilation among the entire section, with maximum AOU ranging from 35 to 50 μmol kg^{-1} at the LSW and ISOW and the remarkable intrusion of oxygenated DSOW (>260 μmol kg^{-1} DO) over the continental slope with AOU ranging from 30 to 40 μmol kg^{-1}. The intermediate and deep layers of the Iceland

and Rockall basins were less ventilated, with AOU values higher than 45-50 µmol kg^{-1}. The thermocline layer placed between 500 and 1000 m depth along these two basins presented the highest maximum AOU throughout the period (>60 µmol kg^{-1}). The stagnation of these waters corresponds with the high C_T and low pH_T (Figures 3a and 2d, respectively) encountered at intermediate depths and should be considered in its temporal evolution.

The temporal distribution and trends of the average physicochemical properties (Figures 4, 5, 6, S4, S5 and S6) revealed remarkable heterogeneities in their interannual evolution within the period 2009-2019 among the different basins and water masses. The interannual trends are presented along with their respective standard error of estimate and correlation factors (r^2 and p-value) in Table 2 and S4. The observed decrease in temperature and salinity, which was more pronounced in subsurface layers, and its implication on the MCS variations were discussed in section 4.

4. Discussion

4.1. Reversal of the physical trends during 2009-2019

The present investigation revealed the cooling and freshening of the upper ocean in the NASPG within the period 2009-2019 (Figure 4; Table 2), as recently reported since the reversal of climatic trend and surface physical properties occurring after 2005 (Holliday et al., 2020; Josey et al., 2018; Robson et al., 2016; Tesdal et al., 2018). The temperature decreased in the upper ocean (with more than 95% level of confidence in SPMW, while non statistically significant in ENACW) by 0.05-0.08 ºC yr^{-1} (Table 2), which is consistent with the ratio of heat loss per decade among the first 700 m depth equivalent to approximately -0.45 ºC decade^{-1} (-0.045 ºC yr^{-1}) encountered over the period 2005-2014 (Robson et al., 2016). The interannual temperature trends in subsurface layers (Table 2) similarly draw the cooling observed in the Irminger basin between 2008 and 2017 (-0.05 and -0.11 ºC yr^{-1} for summer and winter, respectively; Leseurre et al., 2020) and the winter average surface cooling along the entire NASPG between 2004 and 2017 (-0.08 ± 0.02 ºC yr^{-1}; Fröb et al., 2019). The decrement in subsurface salinity (with more than 95% level of confidence in both SPMW and ENACW) of 0.006-0.018 yr^{-1} (Table 2) agreed with the interannual rates provided by Tesdal et al., (2018) for the Irminger basin (-0.007 ± 0.002 yr^{-1}) and for the central-eastern NASPG (-0.020 ± 0.003 yr^{-1}) over the period 2004-2015.

The fluctuations in physical properties were linked to a decrease in oceanic heat transport and storage within the NASPG, which has been attributed to changes in the AMOC over decadal to multidecadal timescales (Balmaseda et al., 2007; Desbruyères et al., 2013; Mercier et al., 2015; Smeed et al., 2018). However, the assessment of the temporal evolution of the AMOC in high latitudes remains uncertain, and there is no evidence of its impact on physical patterns across the NASPG on an interannual scale (Jackson et al., 2022). The changes in the atmospherics forcing also account for the variability of the upper ocean physical properties and can have a cumulative effect over several years (Balmaseda et al., 2007; Böning et al., 2006; Eden and Willebrand, 2001; Marsh et al., 2005).

The distribution of the water mass properties, the processes of vertical and horizontal mixing and the circulation patterns in the Irminger and Iceland basins were described by García-Ibáñez et al., 2016 and 2018. The poleward path of the ENACW (Pollard et al., 1996) and its mixing with waters moving from the west across the NASPG (Ellett et al., 1986) accounted for the highest subsurface temperature and salinity signals observed in the Iceland basin and even more in the Rockall Trough. The SPMW and LSW in the Rockall Trough exhibited higher temperature and salinity signals in the respectively order of ~1ºC and ~0.05-0.1 compared to the Irminger and Iceland basins (Figure 4). The NASPG circulation patterns account for these differences by transporting eastward these water masses, which subduct below the ENACW in the Rockall Trough and mixed with warmer and more saline intermediate waters (i.e. Mediterranean Water) moving from the south (e. g. Ellett et al., 1986; Harvey, 1982; Holliday et al., 2000).

The low temperature and salinity signals in the less-stratified Irminger basin (Figure 2) experienced weaker interannual decreases in subsurface layers and higher rates of cooling and freshening in intermediate and deep waters compared with the Iceland and Rockall basins (Figure 4; Table 2). These longitudinal thermohaline heterogeneities were related to the enhancement of vertical mixing processes in areas of water mass formation along the western NASPG (Fröb et al., 2016; García-Ibáñez et al., 2015; Pickart et al., 2003; Piron et al., 2017) and the water mass transformation along the NAC (Brambilla and Talley, 2008). The strongest decrement in subsurface temperature and salinity along the Iceland and Rockall basins (Figure 4; Table 2) coincided with the significant event of heat loss and freshening observed by

Holliday et al., (2020) in the eastern NASPG over the period 2012-2016, so-called the Great Salinity Anomaly. This pattern was not easily discernible in the Irminger basin due to the transport of freshwater through the Fram Strait, as well as due the redirection of the Labrador Current combined with changing wind stress curl (Holliday et al., 2020).

4.2. Evaluation of the interannual trends in C_T in response to changes in C_{ant} and C_{nat}

The changes in the physical patterns influenced the interannual variability of the MCS. The increase in C_T expected in the upper ocean due to the atmospheric CO_2 uptake was offset by the cooling and freshening (and dealkalinization) of the subsurface layers. The observed rates of increase in C_T (Table 2) did not show notable differences with respect to the interannual trends determined from previous decades at the Irminger and Iceland basins (0.62-0.82 and 0.38-0.64 µmol kg^{-1} yr^{-1}, respectively; García-Ibáñez et al., 2016) and at IRM-TS and IS-TS (0.49-0.71 and 0.39-0.94 µmol kg^{-1} yr^{-1}, respectively; Pérez et al., 2021). The interannual rates of increase in NC_T were higher than those of C_T in the subsurface layers, while the trends were similar among intermediate and deep layers (Table 2). A detailed description of the interannual A_T trends is provided in Appendix B.

The entrance of C_{ant} through the air-sea interface and its accumulation dominated the observed increase in C_T (Figure 5 and Table 2). The increase in ventilation over 2009-2019, shown by the negative AOU trends (Figure S6 and Table S4), favoured the vertical mixing. The upper waters, due to be in contact with the atmosphere and have high biological production rates during the warm months, show high C_{ant} and low C_{nat} contents. The enhanced transport of upper waters toward the interior ocean explained the rapid growth in C_{ant} at intermediate and deep layers. The C_{ant} trends ranged between 0.85 and 1.77 µmol kg^{-1} yr^{-1} (statistically significant at the 99% level). They were higher than the observed on a decadal to multidecadal scale since the late 20th century in the Irminger and Iceland basins (0.21-0.89 µmol kg^{-1} yr^{-1} during 1991-2015,García-Ibáñez et al., 2016; and 0.38-1.15 µmol kg^{-1} yr^{-1} during 1983-2013, Pérez et al., 2021), which show the enhancement in the C_{ant} accumulation on interannual scales during periods of high ventilation, as previously reported by Perez et al., (2008). The C_{nat} show an inverse relationship with C_{ant} at intermediate and deep layers (r^2>0.5; statistically significant at the 95% level of confidence) and weakly decreased across the western deep-convection

NASPG (Figure 5 and Table 2). The growth in phytoplankton biomass (Ostle et al., 2022), together with the enhanced export toward the interior ocean under increasing ventilation, account to the observed decrease in C_{nat} in upper waters. The C_{nat} showed a weaker decrease at intermediate and deep layers due to the dominance of remineralization, which was not intense enough at this time of the year to neutralize the downward transport of low-C_{nat} water from the surface but accounted to partially compensate for its effect. The observed variations in C_{nat} between years were strongly linked with fluctuations in the biological processes explained its non-significant trends at several layers. The changes in the circulation pattern of the NASGP and thus in the horizontal advection related with the climatological forcing (Balmaseda et al., 2007; Desbruyères et al., 2013; Mercier et al., 2015; Thomas et al., 2008; Xu et al., 2013) could behave as a source of variability for both C_{ant} and C_{nat} and also infers differences between consecutive years.

The vertical distribution of C_{ant} and C_{nat} along the transect (Figure 3b and 3c) reflect the higher stratification in the Iceland and Rockall basin compared to the well vertically-mixed Irminger basin. It represents a source of variability in the interannual changes of C_{ant} among the different layers and basins (Figure 4; Table 2). In the western NASPG, the surface heat loss and enhanced deep convection processes favour the solubility and subsequent uptake of atmospheric CO_2 and inject oxygenated and CO_2-rich waters into deeper layers (Messias et al., 2008). Its likely accounts for intermediate and deep layers in the Irminger basin exhibiting the highest C_{ant} accumulation rates in the NASPG (Figure 5; Table 2). The highest ventilation of the interior ocean in the Irminger basin was demonstrated by its minimum AOU values (Figure 2 and S6). It induced a rapid surface-to-bottom transport of C_{ant} shown by its highest rates of increase in intermediate and deep waters throughout the region (Figure 5; Table 2). The high C_{ant} values and its rapidly increment at DSOW were explained by the improved oxygenation of this layer at shallower depths (interannual AOU trends given in Table S4) and its subduction through the continental slope below ISOW.

In the eastern NASPG, the stratification weakened due to the path of the NAC warming eastward the upper water column and accounted to slowdown the increase in C_{ant} in the Iceland basin. An exception comes with the Rockall basin, in which the relatively warm and salty ENACW (Figure 2 and 4) showed the maximum C_{ant} (58-68 µmol kg^{-1}) and minimum C_T

(2120-2131 µmol kg^{-1}) and C_{nat} (2058-2070 µmol kg^{-1}) throughout the region (Figure 3 and 5). The enhanced oxygenation of the ENACW (AOU <20 µmol kg^{-1} and reaching the oxygen saturation after 2014) was related with its high rates of renovation due to its path from the south (Pollard et al., 1996) and its mixing with waters moving eastward (Ellett et al., 1986). This favoured the transport subsurface waters with relatively high C_{ant} content from lower latitudes into the Rockall Trough and introduced wide differences respect to adjacent deeper layers moved from the western NASPG which strength the stratification. As the NAC transports nutrient-rich waters northward and eastward into subsurface layers in the Rockall Trough, biological production tends to increase and actively reduced the CO_2 excess from the ENACW (McGrath et al., 2012b), as proved by the observed low C_T and C_{nat}. The ENACW presented relatively low C_{nat} and C_T (Figure 5) and high A_T and NA_T in 2014. These variations indicated that the increase in carbonate and bicarbonate concentrations rising A_T and NA_T was compensated by the depletion in dissolved CO_2. The relatively high temperature and NA_T in 2014 likely indicated an improved spreading of subsurface waters from subtropical latitudes into the Rockall Trough. The enhanced biological production in these waters, together with the reduction in solubility due to warming which favour the CO_2 evasion to the atmosphere, account for decreasing C_{nat} and thus C_T.

The strong interannual increase in the ENACW ventilation during this decade increase the C_{ant} and decrease the C_{nat} (Rodgers et al., 2009) keeping approximately constant the C_T (Table 2). The poorly ventilated thermocline (AOU > 60 µmol kg^{-1}), placed between 500-1000 m in the eastern NASPG, induced a C_{nat}-driven increase in C_T among the SPMW and uLSW. However, its intrusion does not present relevant variations with time and thus does not introduce differences in the interannual trends of the biogeochemical properties.

4.3. Acidification trends

The interannual pH_T trends (Figure 6, Table 2) exhibited the acidification of the whole water column in NASPG during the period 2009-2019. Despite the acidification rates observed in the most subsurface waters among the three basins were not significant at the 90% confidence level (Table 2), they were consistent in the interval of 0.001 units yr^{-1} to those observed during larger periods at time-series stations located across the North Atlantic: at subtropical latitudes (0.0018 ± 0.0002 units yr^{-1} during 1995-2014 and 0.0020 ± 0.0001 units yr^{-1} during 1995-2023 at ESTOC, González-Dávila and Santana-Casiano, 2023; and 0.0017 ± 0.0001 units yr^{-1} during 1983-2014 at BATS, Bates et al., 2014) and subpolar latitudes (-0.0017± 0.0002 units yr^{-1} at IRM-TS during 1983-2013 and -0.0026 ± 0.0002 units yr^{-1} at IS-TS during 1985-2013, summarized by Pérez et al., 2021). In addition, the changes in the surface pH_T trends has been reported by Leseurre et al., (2020) in the western NASPG within a wide latitudinal area (54-64ºN) during the period 2008-2017 in comparison with the periods 1993-1997 and 2001-2007. Although the highly significant cooling observed in SPMW, the year-to-year variations in ventilation (shown by the annual average AOU and its trends in Figure S6) and thus in C_{nat} and C_{ant} (Figure 5) introduced relevant changes in pH_T on an interannual scale and explained the low significant trends. The extreme negative NAO index of 2009-2010 (Jung et al., 2011) weakened the wind forcing, which infers variability in the circulation patterns and physical properties of the surface waters, consequently reducing deep convection. This was observed in the slowdown in ventilation from 2009 to 2010 (Figure S6) in the Irminger and Iceland basins which caused a relatively increase in C_{nat} and decrease in C_{ant} (Figure 5).

The highest acidification rates were found through intermediate and deep waters in the Irminger and Iceland basins, coinciding with the highest rates of increase in C_{ant} (Table 2, trends statistically significant at more than 95% level of confidence). The exception comes with the DSOW, which presented and interannual decrease in pH_T in phase with those of the uLSW. This singularity was previously observed by García-Ibáñez et al., (2016), which noticed the similar trends between the DSOW and LSW attributed to the recently formation and sink through the continental slope of the DSOW. The acidification rates found among the uLSW, LSW and ISOW (0.0026-0.0032 units yr^{-1}) experienced, on an interannual scale, an acceleration in comparison with previous reported based on long-term records [e. g. 0.0009-0.0017 units yr^{-1} estimated for 1981-2008 by Vázquez-Rodríguez et al., (2012b); 0.0013-0.0016 units yr^{-1} estimated for 1991-2015 by García-Ibáñez et al., (2016); 0.0015-0.0019 units yr^{-1} estimated for 1983-2013 at the IRM-TS by Pérez et al., (2021); 0.0019 ± 0.0001 units yr-1 estimated for 1993-2017 by Leseurre et al., (2020)]. Contrasting the rates of change in pH_T during the decade of study with those encountered by these multidecadal evaluations (and considering the total amount of years comprising each of the studies and the changes in the ion hydrogen concentration- $[H_T^+]$), we estimate an acceleration in the rates of acidification of 0.4-5.4% in the Irminger basin and 1.0-9.0% in the Iceland basin during the 2010s since the late

20th century. This acceleration was mainly attributed to increased deep-water ventilation (shown in the rapid decrease in AOU in Figure S6) favouring the progressively increase in the accumulation of C_{ant} and C_{nat} toward intermediate a deep layers, in which cooling was not significant in the Irminger basin and neither enough intense in both basins to compensate the acidification.

Although the similarities encountered in the pH_T trends among both basins, the average values presented differences which may be closely linked with the transport and transformations of the water masses along the NASPG and mainly modulated by the Reykjanes Ridge (García-Ibáñez et al., 2015, 2016, 2018). The transformation of the SPMW formed in the Iceland (McCartney and Talley, 1982; Brambilla and Talley, 2008; Tsuchiya et al., 1992; Van Aken and Becker, 1996) and flowing with the NAC across the Reykjanes Ridge (Brambilla and Talley, 2008) accounted for the lower pH_T values in the Irminger basin. The differences in pH_T found at intermediate and deep layers were related with the divergence of the LSW path into two cores when it reaches the Reykjanes Ridge (Álvarez et al., 2004; Pickart et al., 2003) and the ISOW path flowing southward along the western Iceland basin and recirculated northward into the eastern Irminger basin (Dickson and Brown, 1994; Saunders, 2001). These differences in the spreading of water masses enhanced the ventilation in the Irminger basin favouring the fall in pH_T compared with the Iceland basin. The rise in the ISOW following the Reykjanes Ridge slope through its eastern flank favoured a strong vertical mixing over and around the ridge (Ferron et al., 2014) and a reduction of the LSW core in the Iceland basin (García-Ibáñez et al., 2015), contributing to resemble pH_T values and trends among the uLSW and LSW in this basin.

The upper waters of the Rockall Trough presented the maximum pH_T throughout the transect (8.02-8.08 units). The observed strong pH_T fluctuations between years related with interannual changes in the NAC do not allow to discern trends with a statistically interval of confidence equal or higher than the 90%. The interannual decrease in pH_T in the ENACW (~0.001 units yr^{-1}) was half than the observed along southernmost transects in the Rockall Trough between 1991 and 2010 (~0.002 units yr^{-1}, McGrath et al., 2012a). The temporal distribution of the average pH_T (Figure 6) highly influenced by the high-ventilation (seen in minimum AOU values highly variables between years and which tend to decrease with 99% statistical confidence; Figure S6 and Table S4) allow to discern two periods: the approximately constant ventilation rates keep a steady state in terms of pH_T during 2009-2011, while the progressively renewal and oxygenation of subsurface waters after 2012 (and peaking in this year) increase the pH_T. The renewal of waters in the shallow Rockall Trough, in contrast with the westernmost NASPG, was not primarily driven by vertical but by lateral advection. The modifications of the ENACW through air-sea exchange and mixing with adjacent waters modulated its properties at different time scales (Holliday et al., 2000) and caused the observed variations in the MCS. The variations in pH_T between consecutive years after 2012 may be attributed to the fluctuations in the spreading into the Rockall Trough of several water masses occupying different depths coming from the south and east (Ellett et al., 1986; Pollard et al., 1996). Holliday et al., 2020 reported the reduction in the spreading of saline subsurface waters from subtropical latitudes and diversion of Arctic freshwater from the western boundary into the eastern NASPG during 2012-2016. The subsequent freshening of the ENACW compensated for the increase in AT expected without the effect of salinity (see in the decreasing AT against the increasing NAT; Figure S4 and Table S4) and weakened the increase in CT expected due to poleward advection (see in the slowdown in the rise of CT in comparison with those of NCT; Figure 5 and S5 and Table 2 and S4). The C_T remains approximately constant (Figure 5 and Table 2) due to the increase in C_{ant} (0.85 ± 0.11 µmol kg^{-1} yr^{-1}; p-value < 0.01) was neutralized by the decrease in C_{nat} (-0.84 ± 0.50 µmol kg^{-1} yr^{-1}; p-value < 0.1). These findings suggest that the atmospheric CO_2 invasion was offset by the growing phytoplankton biomass favouring its biological uptake (Ostle et al., 2022) and the weakening transport of remineralized and saline water from the south (Holliday et al., 2020), thus compensating the acidification of the ENACW.

The SPMW among the Iceland and Rockall basins showed similar pH_T trends (Table 2) due to the emplacement of the poorly-oxygenated thermocline at these depths (García-Ibáñez et al., 2016). The approximately constant AOU at SPMW in the eastern NASPG (Figure S6) proved its steady ventilation, which can introduce differences in the acidification rates among the layers accomplishing the Rockall Trough. The influence of the cooling and freshening of deeper areas due to the spreading and horizontal mixing was notable in the LSW, which presented slightly higher pH_T values in the Rockall respect to the adjacent Iceland basin.

4.4. Interannual changes in Ω_{Ca} and Ω_{Arag}

The analysis of the changes in Ω_{Ca} and Ω_{Arag} hold significance in elucidating the potential effects of OA over the $CaCO_3$ species calcite and aragonite, thereby offering insights into their potential implications for marine calcifying organisms and ecosystems. The vertical distribution of Ω_{Ca} and Ω_{Arag} is presented in Figure S3. The upper and intermediate layers up to 2100-2400 m depth of the Irminger and Iceland and the whole Rockall basin were supersaturated for aragonite (Ω_{Arag} >1), while the DSOW was undersaturated (Ω_{Arag}<1). The ISOW, with Ω_{Arag} ranged between 1.0 and 1.1 at the beginning of the decade, crossed to undersaturated conditions at the end of the period due to the progressively rise of the aragonite saturation horizon (depth in which Ω_{Arag}=1). The whole water column throughout the section was supersaturated for calcite (Ω_{Ca}>1) due to its lower solubility (Mucci, 1983). The Ω_{Ca} and Ω_{Arag} in the SPMW (2.2-2.7 and 1.4-1.7 units, respectively) were lower than the encountered equatorward in the subsurface Atlantic (>4.0 and >2.5 units, respectively; González-Dávila et al., 2010; González-Dávila and Santana-Casiano, 2023). The poleward pathway of low-latitude upper waters through the Rockall Trough explained the higher Ω_{Ca} and Ω_{Arag} found in the ENACW (3.0-3.6 and 1.8-2.3 units, respectively). The reduction in Ω_{Ca} and Ω_{Arag} towards higher latitudes in upper and intermediate layers smooth the vertical gradients in the NASPG compared with the subtropical latitudes (González-Dávila et al., 2010; González-Dávila and Santana-Casiano, 2023).

The correlation of Ω with pH_T (r^2=0.90) with a level of significance higher than the 99% explained that the individual components driving OA accompanied the declining in Ω. The interannual trends in Ω_{Ca} and Ω_{Arag} (Figure 7, Table 2) exhibited the decrement through the whole water column along the NASPG with a level of statistical confidence generally higher than the 90%. The rates of declining for Ω_{Ca} and Ω_{Arag} in the SPMW (0.011-0.021 and 0.007-0.013 units yr-1; respectively) were consistent with the trends observed up to 100 m depth at ESTOC between 1995 and 2023 (0.019 ± 0.001 and 0.012 ± 0.001 units yr^{-1}, respectively; González-Dávila and Santana-Casiano, 2023) and in surface waters at the IS-TS between 1985 and 2008 (0.0117 ± 0.0011 and 0.0072 ± 0.0007 units yr^{-1}, respectively; Olafsson et al., 2009). The Ω_{Arag} trend estimated for SPMW in the Irminger basin (-0.007 ± 0.003 units yr^{-1}) is consistent with that reported for surface waters by Bates et al., (2014) over 1983-2014 (-0.008

± 0.004 units yr^{-1}) and fall within the range of those estimated during summer by Leseurre et al., 2020 over 2008-2017 (-0.005 ± 0.001 units yr^{-1}). Chau et al., 2014 recently deduced from reconstructed products a slower decrease (-0.004 ± 0.001 units yr^{-1}), highlighting the large uncertainty in the estimations of interannual trends for pH and Ω_{Arag} across the NASPG due to the low-data sampling frequency at their monitoring sites. The declining in Ω_{Arag} in the SPMW accelerated by ~26% and ~51% in the Irminger and Iceland basins, respectively, in comparison with the trends given for the period 1991-2018 (0.0052 ± 0.0006 and 0.0049 ± 0.0015 units yr^{-1}, respectively; García-Ibáñez et al., 2021). The observed decrease in Ω_{Arag} in the SPMW was ~23% faster in the Rockall Trough than in the adjacent Iceland basin. The interannual declining for Ω_{Ca} and Ω_{Arag} in the ENACW (0.012 and 0.008 units yr^{-1}, respectively) agreed with these previous observations but were not statistically significances likely due to the high variability modifying the changes in pH_T in this layer (see section 4.2). Despite the acceleration of the acidification rates toward intermediate and deep layers, the declining rates weakened for Ω_{Ca} and even more for Ω_{Arag} (Table 2). Moreover, the vertical profiles were approximately constant throughout the section in contrast with the heterogeneous vertical distribution of pH_T between basins. This behaviour was previously observed in the Irminger and Iceland basins by García-Ibáñez et al., (2021) and explained by pressure and temperature-induced changes in the speciation of the CO_2-carbonate chemistry species (Jiang et al., 2015) and in the solubility of calcite and aragonite (Mucci, 1983). Their combined action counterbalanced the alterations in Ω resulting from acidification, particularly in colder deep waters where the solubility of calcite and aragonite was reduced (García-Ibáñez et al., 2021). However, the fall down in Ω_{Ca} and Ω_{Arag} along the uLSW, LSW and ISOW accelerated by 40-75% in relation with the trends reported by García-Ibáñez et al., (2021) for the Irminger and Iceland basins. The LSW and ISOW presented faster declining rates for Ω_{Ca} and Ω_{Arag} in the Irminger (Table 2), which may be caused by the enhanced ventilation of the interior ocean which accelerated the acidification (see section 4.2). The westward rise in depth of these layers along the Greenland continental slope, accompanied by a subsequent elevation in the horizons of solubility, resulted in reduced buffering capacity against acidification effects in the Irminger basin when compared to the Iceland basin. In contrast, the rise in depth of LSW in the Rockall Trough favour the increment of ~0.2 units in Ω_{Ca} and ΩArag with respect to the Iceland basin but had not influence on the interannual trends, which were coinciding. The Ω_{Ca} and Ω_{Arag} in the DSOW, despite showed a trend accelerated by ~30% compared to the observed by García-Ibáñez et al., (2021), presented the weakest interannual decreases throughout the section (0.004 ± 0.003 and 0.002 ± 0.001 units yr^{-1}, respectively) due to the high pressure and low temperatures compensating the rapidly acidification (Figure 6, Table 2).

The decrease in Ω could have severe consequences on organisms reliant on aragonite, which is less resistant to dissolution than calcite (Mucci, 1983; Broecker and Peng, 1983) and thus expected to experience relatively higher susceptibility to the effects of OA over shorter time scales (Raven et al., 2005). The progressive reduction in Ω_{Arag} is driving a long-term decrease in the depth of the aragonite saturation horizon (Ω_{Arag}=1) by 80-400 m since the preindustrial era (Álvarez et al., 2003; Feely et al., 2004; Pérez et al.,2013, 2018; Pérez et al., 2013; Tanhua et al., 2007; Wallace, 2001) and is projected to shoal by more than 2000 m by the end of the century under the IS92a scenario (Orr et al., 2005). The vertical section of Ω_{Arag} in Figure S3 shows the shallower aragonite saturation horizon during 2009 and 2016 compared to preindustrial times. Likewise, Orr et al., (2005) suggested that high-latitudes surface waters could become undersaturated when the atmospheric CO_2 concentration double the preindustrial concentration within the next 50 years. It would reduce the calcification rates in some shallow calcifying organism by more than the 50% (Feely et al., 2004).

The planktonic aragonite-producers pteropods (e. g. *Limacina helicina, Clio pyramidata*), which have high population densities in subpolar regions up 300 m depth (Bathmann et al., 1991; Urban-Rich et al., 2001) and play a key role in the export flux of both carbonate and organic carbon (Accornero et al., 2003; Collier et al., 2000), are expected to be highly vulnerable to OA if the aragonite saturation horizon continue to shoal (Orr et al., 2005). The undersaturation toward intermediate and upper layers negatively influence the aragonite-based CWC (e. g. *Lophelia pertusa, Madrepora oculate*), which show their highest diversity and population along the NASPG between 200 and 1000 m depth among the global ocean (Roberts et al., 2009). In fact, several studies reported that CWC ecosystems are anticipated to be among the first deep-sea ecosystems to experience acidification threats (Gehlen et al 2014; Guinotte et al., 2006; Maier et al., 2009; Raven et al., 2005; Roberts et al., 2009; Turley et al., 2007), particularly in the North Atlantic (Perez et al., 2018). The findings presented here contribute to a deeper understanding of the biological impacts of OA along the NASPG.

4.5. Processes controlling OA and Ω trends

Due to the variety of processes involved in OA, a decomposition of the pH_T and Ω trends into the individual components that govern their spatio-temporal variability was done (see section 2.2.6). The interannual variations in pH_T ($\frac{dpH_T}{dt}$) and Ω ($\frac{d\Omega}{dt}$) explained by fluctuations in temperature ($\frac{\partial pH_T}{\partial T}\frac{\partial T}{dt}$ and $\frac{\partial \Omega}{\partial T}\frac{\partial T}{dt}$) , salinity ($\frac{\partial pH_T}{\partial S}\frac{\partial S}{dt}$ and $\frac{\partial \Omega}{\partial S}\frac{\partial S}{dt}$), A_T ($\frac{\partial pH_T}{\partial A_T}\frac{\partial A_T}{dt}$ and $\frac{\partial \Omega}{\partial A_T}\frac{\partial A_T}{dt}$) and C_T ($\frac{\partial pH_T}{\partial C_T}\frac{\partial C_T}{dt}$ and $\frac{\partial \Omega}{\partial C_T}\frac{\partial C_T}{dt}$) were calculated for each layer and basin (Eq. 2) and summarized in Table 3 and 4. The positive contributions of each of the drivers indicate increments while negative contributions the opposite. The cumulative changes resulting from the distinct drivers (referred to with the subscript "calculated" in Table 3 and 4) were consistent with the observed pH_T trends (referred to with the subscript "obs" in Table 3 and 4), thereby instilling confidence in the methodology. An exception was found at the DSOW, in which the strong NA_T decrease had a crucial influence on declining Ω.

The minimal differences between observed and calculated rates of change have added coherence to the non-significant trends identified for pH_T and Ω trends and/or its drivers in some basins and layers (Table 2, 3 and S4). In the entire section at SPMW, the $\frac{dpH_T}{dt}$ (calculated), explained by the cumulative impact of its drivers (all of them statistically significant at the 95% level of confidence), aligns within a range of <0.0002 units yr^{-1} with $\frac{dpH_T}{dt}$ (obs) (which was not significant). In the Irminger and Iceland basins at intermediate and deep layers, the $\frac{dpH_T}{dt}$ (obs) (statistically significant at least at the 95% level of confidence) were consistent within the range of <0.001 units yr^{-1} with $\frac{dpH_T}{dt}$ (calculated) (T, S and NA_T shows non-significant trends at some of the intermediate and deep layers). The interannual variations were non-significant for pH_T neither for its drivers in the Rockall Trough at LSW and ENACW. The high temporal dispersion of average data in these layers was mainly related to the rise in depth of LSW along the eastern continental slope and its mixing with shallower waters coming from subtropical latitudes (Ellett et al., 1986; Harvey, 1982; Holliday et al., 2000). The substantial variability in the Rockall Trough made it difficult to discern OA patterns and its drivers on an interannual scale. Therefore, long-term monitoring and the development of multidecadal-scale studies are required in this area to derive significant conclusions.

The cooling and freshening modified the physical-driven pH_T changes compared with those encountered by García-Ibáñez et al., (2016) during previous decades in the western NASPG. The cooling contributed to increase the pH_T and compensated the observed acidification rate. The increase in pH_T due to temperature fluctuations was maximum at SPMW (~0.001 units yr^{-1}) and negligible in deeper layers (<0.0003 units yr^{-1} at uLSW and below). The increase in pH_T due to salinity fluctuations was minimal (<0.0001 units yr^{-1}) through the whole water column in the three basins, reflecting that the observed freshening caused insignificant changes in pH_T. The temperature and salinity contributed by 19.1-26.5% and 1.2-3.3%, respectively, in the total pH_T change in the upper layers, while presented an influence three times lower toward the interior ocean (1.3-7.6% and <0.6%, respectively). The enhanced convective processes in the Irminger basin (e. g. Fröb et al., 2016; García-Ibáñez et al., 2015; Gladyshev et al., 2016a, 2016b; Piron et al., 2017) together with the rapid transport of LSW from the Labrador Sea to the Irminger basin (Yashayaev et al., 2007) introduced differences in the thermal-driven pH_T with the Iceland basin, as previously reported by García-Ibáñez et al., (2016). The advection of LSW through the Greenland continental slope also affected the DSOW (Read, 2000; Yashayaev and Dickson, 2008), which shows thermal-driven pH_T changes consistent with those encountered through the LSW in the Irminger basin.

Despite the negligible direct contribution of the salinity fluctuations over the pH_T changes, the freshwaters fluxes influence the distribution of A_T and C_T indirectly affecting pH_T trends. After removing salinity effects, NA_T show positive trends in subsurface layers and negative trends toward the interior ocean (Figure S4 and Table S4; detailed in Appendix B). The changes in NA_T described the 7.8-10.1% of the total pH_T change at SPMW. The NA_T-driven pH_T changes weakened with depth (Table 3) due to the insignificantly interannual changes in NA_T through LSW and ISOW (Table S4). The weak contribution of NA_T in these layers (1.3-5.1%) could be related to the difficulty of reversing the large alkalinization until the 2000s resulted from the slowdown in the formation of LSW since the mid-90s (Lazier et al., 2002; Yashayaev, 2007), which was transmitted towards deeper overflow waters (Sarafanov et al., 2010). The substantial interannual changes and the abrupt change between periods of increase and decrease of the seawater properties at DSOW (Yashayaev et al., 2003; Stramma et al., 2004) linked with changes in the LSW formation (Dickson et al., 2002) explained the rapidly decrease in NA_T (Table S4), which described the 14.6% of the pH_T declining.

The increase in NC_T drove by the rise in C_{ant} was found to govern the acidification, with a contribution higher than the 67% across the entire water column. The NC_T-driven pH_T declining was close to twice the observed and calculated acidification rates through the SPMW (Table 3). However, the contribution of NC_T at SPMW (67-69%) was lower than the encountered toward the interior ocean (82-96%) due to the relevance of temperature and A_T over pH_T trends in the upper layers. The cooling and increase in NA_T counteracted the acidification expected by the increasing C_T at SPMW by 28-34% and 11-15%, respectively. In intermediate and deep layers, the thermal-neutralization of the C_T-driven acidification was weaker (1.5-9.3%) and the decreasing NA_T contributed to decrease the pH_T by < 15%. Freshening played a minor role in countering acidification (<6% in upper layers and <2% in the interior ocean).

In line with declining pH_T, 79-83% of the decrease in Ω in subsurface layers was attributed to the C_{ant}-driven rise in NC_T, with this influence reaching up to 97% in deeper waters. The increase in NA_T in the SPMW accounted by 10.4-13.0% in the Ω trends and counteracted its NC_T-driven decrease by 12.6-16.2%. The contribution of NA_T fall and reversed toward deeper waters, explained <6% of the decline in Ω in the uLSW, LSW and ISOW in the Irminger basin and <11% in the Iceland basin. The pronounced impact of the rapid decrease in NA_T on the acidification of the DSOW (see section 4.3) depicted the greater contribution of NA_T encountered among the Irminger basin (16%) and compensated the NC_T-driven decrease in Ω by 36.4%. In the Rockall Trough, the contribution of NC_T changes on Ω was reduced at LSW (78.2-79.0%) compared to the Irminger basin (94.5%) while the effect of NA_T fluctuations tripled until reach 12.6-12.7%.

Despite the crucial role of cooling in mitigating acidification, temperature fluctuations have an opposite effect on Ω due to the thermodynamic relationship inherent in the acid-base equilibrium of the CO_2-carbonate system (Dickson and Millero, 1987). In the Irminger and Iceland basins, the observed decrease in temperature contributed negligibly to the decline in Ω (3.6% in the SPMW and less than 2% in intermediate and deep waters). The influence of salinity, as with the pH_T trends, was minimal: the observed freshening slightly elevated the Ω trends, offsetting the decline by 4.6-4.7% in the SPMW, 1.1-2.1% in the uLSW and LSW, and 0.5-1.2% in the ISOW and DSOW. Even with the slightly faster cooling and freshening observed in the Rockall Trough, the contributions of temperature and salinity to Ω did not exceed 7% in any of its layers.

5. Conclusions

This research has evaluated the interannual changes in the basin-wide MCS dynamics along the NASPG during 2009-2019. Despite the observational period is relatively short to quantify long-term trends and to formulate significant future projections, the finding has allowed to evaluate the ocean response, in terms of MCS dynamics and on an interannual scale, to changes in deep-water convection and to isolate events affecting the physical patterns. The assessment of OA within the Irminger and Iceland basins was enhanced by supplying novel data and trends spanning a decade in which the physical patterns reversed. Additionally, the study provides an unprecedent analysis of the physico-chemical variations in the Rockall Trough, which is crucial for the assessment of the entire longitudinal span of the NASPG. It facilitates a more accurate understanding of the mechanisms dictating basin-scale acidification processes and advances our understanding of OA in the North Atlantic and Global Ocean.

Overall, the entrance and accumulation of C_{ant} and interannual acidification trends were strongly affected by the cooling, freshening and enhancement in the oxygenation during this decade. The longitudinal span of the NASPG and the differences in circulation patterns, water masses and bathymetry behaved as a source of spatio-temporal variability. The interannual acidification trends of the main water masses across the NASPG ranged between 0.0006-0.0032 units yr-1 and caused a decline in the ΩCa and ΩArag of 0.004-0.021 and 0.003-0.013 units yr-1, respectively. The convective processes increased the accumulation rates of Cant in the interior ocean by 50-86% and accelerated the acidification rates by around 10% compared to previous decades in the Irminger and Iceland basins. The shallower hydrography of the Rockall Trough and the poleward circulation patterns accounted for differences in the acidification rates respect to surrounding waters.

The Cant-driven increase in NCT was found to govern the acidification of the NASPG with contributions exceeding 60%. The combined effect of the decreasing temperature, salinity and NAT neutralized close to one-half of the acidification along the entire longitudinal span of the SPMW. The enhanced deep-water ventilation in the western NASPG slowdown the cooling and freshening toward the interior ocean, weakening the physical counterbalance of acidification.

The present investigation emphasizes the progressively increase in the uptake and accumulation of Cant and subsequent acceleration of OA along the NASPG. Novel data and results provided could be compared with other repeated hydrographic section data at mid and high latitudes in the North Atlantic, such as the A02, A25, AR07E and AR28 framed in the GO-SHIP program, as well as used in conjunction to develop future investigations. Additionally, they contribute to the improvement of the projections pertaining to the future state of the oceans run by models and forecast. Considering the important variability in the mechanism controlling the distribution of the physico-biogeochemical properties and particularly the OA in the North Atlantic, this research aims to highlight the necessity of continue monitoring and sampling the whole water column through repeated hydrographic sections, especially through the highly variable but less assess easternmost part.

Appendix A: Correction of Dissolved Oxygen records for the cruise of 2019

The sensor-measured DO data for the cruise of 2019 were corrected by considering the DO output data given by the neural network ESPER_NN (Carter et al., 2021) for the cruises of 2016 and 2019 (hereinafter ESPER-estimated DO) and the WINKLER-measured DO during the cruise of 2016. Among the 16 equations provided by the ESPER_NN that differently combines seawater properties as predictors, we use the equation 8 which only need as inputs the T and S (due to lack of measured macronutrients during the cruise of 2019) along with latitude, longitude, depth and date (see Table 2 in Carter et al., 2021). The reported Root Mean Squared Error (RMSE) of equation 8 for DO estimations in the global ocean is ± 9.7 μmol kg-1, which is reduced for intermediate waters (1000-1500 m) to ± 5.9 μmol kg^{-1} (see Table 7 in Carter et al., 2021). Additionally, a new set of DO for 2019 based on WINKLER data for 2016 was computed, which was referred in this study as "pseudo-WINKLER" data. The difference between WINKLER-measured and ESPER-estimated DO during 2016 was interpolated to the longitudes and depths of the samples of 2019 by applying Delaunay Triangulation. The pseudo-WINKLER data was described as the sum of these interpolated differences and the ESPER-estimated DO data for 2019. The longitudinal distribution of measured and ESPER-estimated DO data for 2016 and 2019 is depicted in Figure S1a and S1b. The interpolated pseudo-WINKLER data for the cruise of 2019 were included in Figure S1a.

The sensor records of DO in 2019 were in average 4.90 μmol kg^{-1} lower than the ESPER-estimated and 10.31 μmol kg^{-1} lower than the pseudo-WINKLER. A higher discrepancy was observed in the average sensor-measured DO in the east part (237.60 ± 15.00 μmol kg^{-1}) compared with the west part (281.40 ± 14.75 μmol kg^{-1}). The average differences (measured minus ESPER-estimated DO and measured minus pseudo-WINKLER DO, $\Delta DO_{\text{meas-ESPER}}$ and $\Delta DO_{\text{meas-pseudoWINLKER}}$, respectively; Figure S2c and S1d) shows that the sensor records were strongly underestimated in the east part (-20.98 ± 10.91 and -28.77 ± 12.60 μmol kg^{-1}, respectively) and weakly overestimated in the west part (8.59 ± 8.53 and 5.18 ± 12.02 μmol kg^{-1}, respectively) during the cruise of 2019. These differences were corrected separately west and east of 21.5ºW by using the relationship $\frac{\Delta DO_{meas-pseudoWINKLER}}{measured\ DO}$. The averages of this relationship in the west and east part of the transect (0.016 and -0.12 μmol kg^{-1}, respectively) were used as corrector factors. The corrected DO values were given by the product between the measured DO and $\left(1 - \frac{\Delta DO_{meas-pseudoWINKLER}}{measured\ DO}\right)$.

Appendix B: Interannual trends of *A_T* and *NA_T*

The interannual trends of A_T (Figure S4 and Table S4) was found to be highly impacted by freshening, with decreasing rates ranging from -0.33 to -0.71 μmol kg^{-1} yr^{-1} among the SPMW and ENACW and from -0.01 to -0.18 μmol kg^{-1} yr^{-1} within the uLSW, LSW, ISOW and DSOW. It contrasts with the minimal interannual changes and slight rates of increase in A_T encountered among the different layers by García-Ibáñez et al., (2016) from 1991 to 2015 in the Irminger basin (between 0.10 and 0.28 μmol kg^{-1} yr^{-1}) and Iceland basin (between -0.04 and 0.07 μmol kg^{-1} yr^{-1}), and with the trends reported for the period 1983-2013 by Pérez et al., (2021) at the IRM-TS (between 0.13 and 0.22 μmol kg^{-1} yr^{-1}) and at the IS-TS (between -0.04 and 0.15 μmol kg^{-1} yr^{-1}). These heterogeneities in the temporal evolution of the A_T were driven by the decadal salinification of the whole water column observed since the late 20th century and interrupted by interannual freshening episodes such as during the 2010s.

The interannual increase in NA_T in upper layers could be related to acidification, which favour the dissolution of carbonates, combined with increasing biological production reported for upper layers across the NASPG (Ostle et al, 2022). It contrasts with the constant to weakly decrease in NA_T at intermediate and deep layers, in which the accelerated acidification was compensated by the dominance of remineralization processes over lower biological uptake. Consequently, the positive NA_T trends encountered in the upper layers lead a rise in pH_T, while the diminished NA_T contributed to decrease the pH_T toward the interior ocean.

The A_T/S relationship has increased at a rate of 0.5 ± 0.2 µmol kg^{-1} yr^{-1} (p-value < 0.05) due to the combined action of the freshening (Figure 4) and the progressive increase of A_T-rich water inflows through upper layers (observed in the positive trends of NA_T in SPMW and ENACW; Figure S4). This was likely associated with the stagnation of A_T-rich subtropical waters in the upper layers due to the slowdown of the NASPG since the mid-90s (e.g., Böning et al., 2006; Häkkinen and Rhines, 2004), along with changes in the spreading of waters from higher latitudes influenced by melting.

Code Availability

MATLAB and R codes for CANYON-B are available at https://github.com/HCBScienceProducts/CANYON-B. MATLAB and R code for ESPER_NN are available at https://github.com/BRCScienceProducts/ESPER. MATLAB code for anthropogenic carbon calculation is available at http://oceano.iim.csic.es/_media/cantphict0_toolbox_20190213.zip. The CO_2SYS programme for MATLAB is available at https://github.com/jonathansharp/CO2-System-Extd.

Data Availability Statement

The measured surface-to-bottom CLIVAR data (2009-2019) used in this investigation are published in open-access at Zenodo (DOI: 10.5281/zenodo.10276221). The GO-SHIP A25-OVIDE data for the cruise of 2018 is available at SEANOE (https://www.seanoe.org/data/00762/87394/).

Author contribution

DCH contributed with data analysis and wrote the manuscript. FFP, DCH, AV, DGS, AGG, MGD and JMSC worked on the design, conceptualization and data preparation. SG, AS, MGD, JMSC, AGG and DGS participated in 8, 4, 7, 7, 2 and 2 cruises, respectively. SG and AS were the Chief Scientist in all cruises and responsible for the operational and maintenance procedures for the CTD and additional sensors and thus for physical and sensor-measured variables. MGD and JMSC got the funding acquisition and provision of resources for the Spanish team from the ULPGC. SG and AS got the funding for ship time and provision of resources for all the cruise participants. All authors critically revised the manuscript.

Competing interest

The authors declare that the research was conducted in the absence of any commercial or financial relationships that could be construed as a potential conflict of interest.

Acknowledgement

The participation on the cruises for the Spanish Team from the ULPGC was funded by the Science Spanish Ministry under the Complimentary Actions CTM2008-05255, CTM2010-09514-E and CTM2011-12984-E (years 2009-2011), the FP7 European project CARBOCHANGE under grant agreement no. 264879 and by the Spanish Innovation and Science Ministry through the Projects EACFe (CTM2014-52342-P) and ATOPFe (CTM2017-83476-P). SG and AS were supported by FMWE-2023-0002. FFP and AV were supported by the BOCATS2 (PID2019-104279GB-C21) project funded by MCIN/AEI/10.13039/501100011033 and by EuroGO-SHIP project (Horizon Europe #101094690). The participation of DCH was funded by the PhD grant PIFULPGC-2020-2 ARTHUM-2. Special thanks go to the technician and researchers Adrian Castro Álamo (2 cruises), Anna Barrera Galderique (3 cruises), Rayco Alvarado Medina (2 cruises) and Pilar Aparicio Rizzo (1 cruise) who helped with in situ analysis. We also thanks technicians at the P. P. Shirshov Institute of Oceanology from the Russian Academy of Science for the in situ analysis of dissolved oxygen and nutrients.

Legend for figures

Figure 1. (a) Map of the North Atlantic Subpolar Gyre (NASPG) with the schematic diagram of the surface and deep circulation patterns compiled from Lherminier et al., (2010); Pérez et al., (2021); Sarafanov et al., (2012); Schmitz and McCartney, (1993); Schott and Brandt, (2007) and Sutherland and Pickart, (2008). The acronyms are defined as follow: the bathymetric features are shown in grey (RR: Reykjanes Ridge, HB: Haton Bank, GBB: George Bligh Bank, CGFZ: Charlie-Gibbs Fracture Zone, GIR: Greenland-Iceland Ridge, and GSR: Greenland-Scotland Ridge), the surface currents are shown in orange (NAC: North Atlantic Current, and IC: Irminger Current) and the deep water circulation is shown in blue and purple (ISOW: Iceland-Scotland Overflow Water, DSOW: Denmark Strait Overflow Water, LSW: Labrador Sea Water, and DWBC: Deep Western Boundary Current). The longitudinal distribution of the surface-to-bottom sampling stations along the cruise track of 2016 (repeated throughout the cruises) is shown with red dots. The black lines along the cruise track delimited the three basins. (b) Vertical distribution of the water masses considered in this study for each of the basins. The isopycnals, plotted over the salinity distribution for the cruise of 2016, show the limits of the layers and were defined by potential density (in kg m^{-3}) referred to 0 dbar (σ_0). The vertical gray lines show the limits between basins. The acronyms of the water masses and the selection of potential density values delimiting the layers are detailed in section 2.2.4. Figure produced with Ocean Data View (Schlitzer, 2021).

Figure 2. Water-column distribution along the longitudinal transect of (a) temperature, (b) salinity, (c) A_T, (d) pH_T andI) AOU for the cruises of 2009 (left plots) and 2016 (right plots). The vertical while lines show the limits between basins. Figure produced with Ocean Data View (Schlitzer, 2021).

Figure 3. Water-column distribution along the longitudinal transect of (a) C_T, (b) C_{ant} and (c) C_{nat} for the cruises of 2009 (left plots) and 2016 (right plots). The vertical while lines show the limits between basins. Figure produced with Ocean Data View (Schlitzer, 2021).

Figure 4. Temporal distribution (2009-2019) of the average temperature and salinity in each of the layers considered for the Irminger (left plot column), Iceland (central plot column) and Rockall basins (right plot column). The average values were calculated for each cruise and layer and represented with coloured points together with their respective error bars at the time of each cruise (the method used for calculations was described in section 3.2). In the Irminger plots, the empty points represent the average values for 2019 calculated with the measured data available in the easternmost part of the basin (sampled part during this cruise), while the coloured points for 2019 represent the average values corrected with A25-OVIDE-2018 data. The interannual trends were given by linear regression of the average values, with the values of the slope, the standard error of estimate and the r^2 presented in Table 2.

Figure 5. Temporal distribution (2009-2019) of the average C_T, C_{ant} and C_{nat} in each of the layers considered for the Irminger (left plot column), Iceland (central plot column) and Rockall basins (right plot column). The average values were calculated for each cruise and layer and represented with coloured points together with their respective error bars at the time of each cruise (the method used for calculations was described in section 3.2). In the Irminger plots, the empty points represent the average values for 2019 calculated with the measured data available in the easternmost part of the basin (sampled part during this cruise), while the coloured points for 2019 represent the average values corrected with A25-OVIDE-2018 data.

The interannual trends were given by linear regression of the average values, with the values of the slope, the standard error of estimate and the r^2 presented in Table 2.

Figure 6. Temporal distribution (2009-2019) of the average pH_T (in situ temperature) in each of the layers considered for the Irminger (left plot column), Iceland (central plot column) and Rockall basins (right plot column). The average values were calculated for each cruise and layer and represented with coloured points together with their respective error bars at the time of each cruise (the method used for calculations was described in section 3.2). In the Irminger plots, the empty points represent the average values for 2019 calculated with the measured data available in the easternmost part of the basin (sampled part during this cruise), while the coloured points for 2019 represent the average values corrected with A25-OVIDE-2018 data. The interannual trend were given by linear regression of the average values, with the values of the slope, the standard error of estimate and the r^2 presented in Table 2.

Figure 7. Temporal distribution (2009-2019) of the average ΩCa and ΩArag in each of the layers considered for the Irminger (left plot column), Iceland (central plot column) and Rockall basins (right plot column). The average values were calculated for each cruise and layer and represented with coloured points together with their respective error bars at the time of each cruise (the method used for calculations was described in section 3.2). In the Irminger plots, the empty points represent the average values for 2019 calculated with the measured data available in the easternmost part of the basin (sampled part during this cruise), while the coloured points for 2019 represent the average values corrected with A25-OVIDE-2018 data. The interannual trends were given by linear regression of the average values, with the values of the slope, the standard error of estimate and the r^2 presented in Table 2.

Legend for Tables

Table 1. Metadata list of hydrographic cruises.

Table 2. Interannual trends of temperature, salinity, C_T, C_{ant}, C_{nat}, pH_T, ΩCa and ΩArag in each of the layers and basins. The ratios of change were based on linear regressions applied to the average values (as represented in Figures 4-7) and presented together with its Standard error of estimate. The correlation coefficients r^2 and p-values were also provided. Values in bold denote trends statistically significant at the 95% level of confidence.

Table 3. Temporal changes in pH_T (**in 10^{-3} units yr^{-1}**) explained by fluctuations in temperature $\left(\frac{\partial pH_T}{\partial T}\frac{\partial T}{dt}\right)$, salinity $\left(\frac{\partial pH_T}{\partial S}\frac{\partial S}{dt}\right)$, A_T $\left(\frac{\partial pH_T}{\partial A_T}\frac{\partial NA_T}{dt}\right)$, and C_T $\left(\frac{\partial pH_T}{\partial C_T}\frac{\partial NC_T}{dt}\right)$ in each of the layers considered for the Irminger, Iceland and Rockall basins during the period 2009-2019. The sum of changes explained by the individual drivers represents the calculated interannual pH_T change $\left(\frac{dpH_T}{dt}\text{ calculated}\right)$, as detailed in section 2.2.5. The observed interannual pH_T trends $\left(\frac{dpH_T}{dt}\text{ observed}\right)$, shown in Figure 7 and provided in Table 2, were also added to the table for comparison.

Table 4. Temporal changes in ΩCa and ΩArag (**in 10^{-3} units yr^{-1}**) explained by fluctuations in temperature $\left(\frac{\partial \Omega}{\partial T}\frac{\partial T}{dt}\right)$, salinity $\left(\frac{\partial \Omega}{\partial S}\frac{\partial S}{dt}\right)$, A_T $\left(\frac{\partial \Omega}{\partial A_T}\frac{\partial NA_T}{dt}\right)$, and C_T $\left(\frac{\partial \Omega}{\partial C_T}\frac{\partial NC_T}{dt}\right)$ in each of the layers considered for the Irminger, Iceland and Rockall basins during the period 2009-2019. The sum

of changes explained by the individual drivers represents the calculated interannual Ω change $\left(\frac{\mathrm{d}\Omega}{\mathrm{dt}}\ \mathrm{calculated}\right)$, as detailed in section 2.2.6. The observed interannual Ω trends $\left(\frac{\mathrm{d}\Omega}{\mathrm{dt}}\ \mathrm{observed}\right)$, shown in Figure 6 and provided in Table 2, were also added to the table for comparison.

Figures

Fig. 1

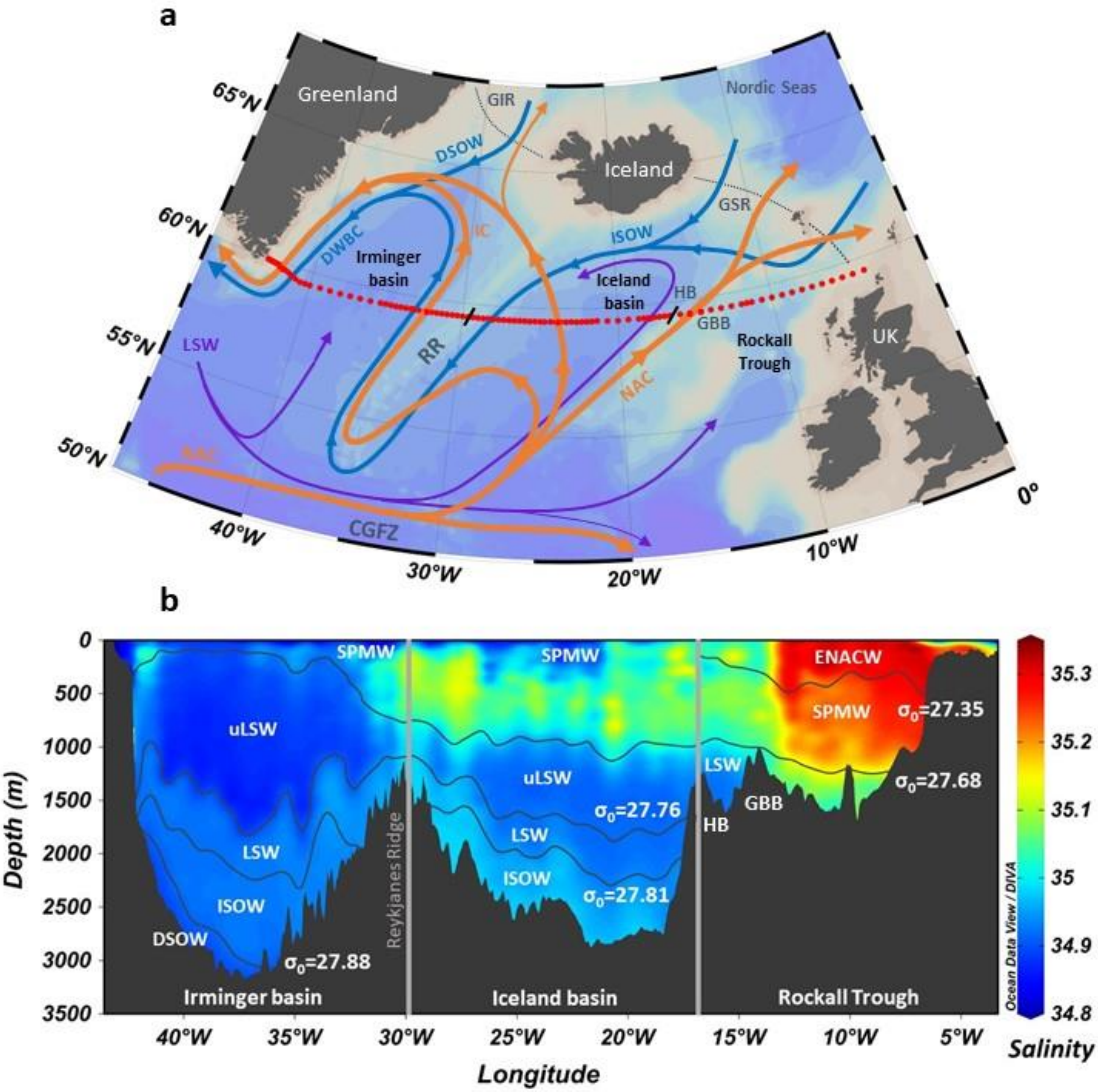

Fig. 2

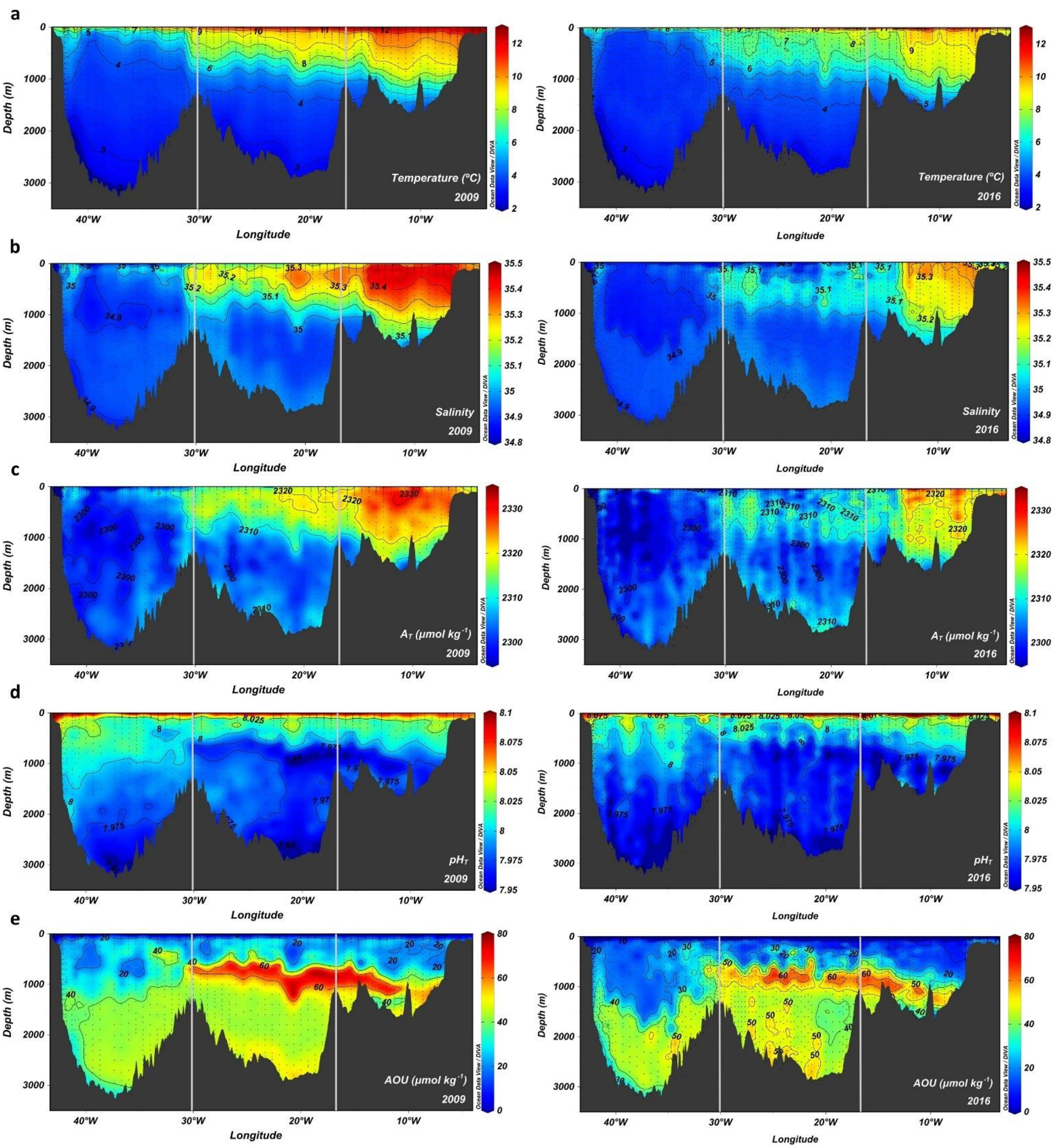
a
b
c
d
e
Depth (m)
Longitude
40°W
30°W
20°W
10°W
Temperature (ºC)
Salinity
A_T (μmol kg^{-1})
pH_T
AOU (μmol kg^{-1})
2009
2016
Ocean Data View / DIVA

Fig. 3

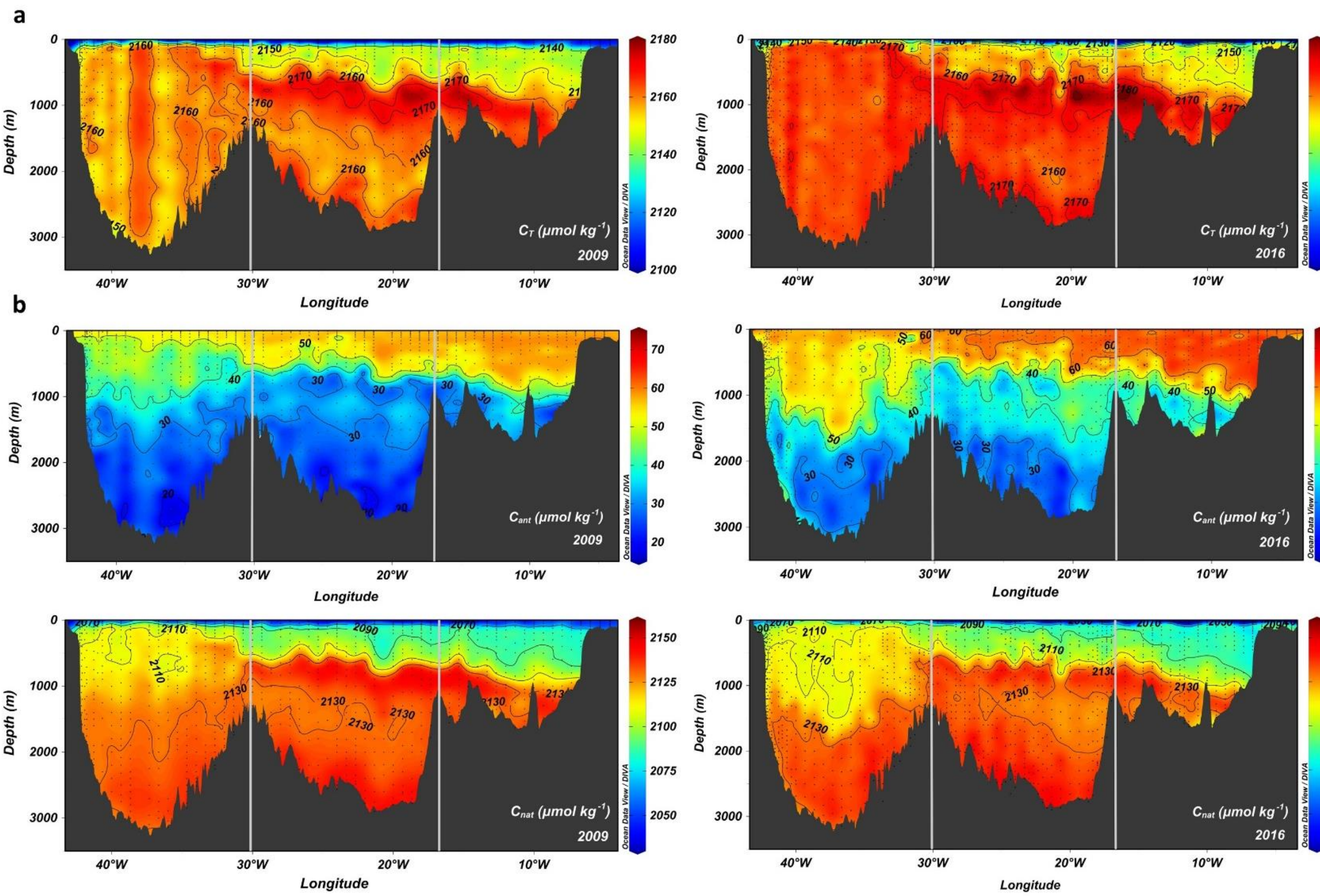
a
b
Depth (m)
Longitude
40°W
30°W
20°W
10°W
C_T (µmol kg^{-1})
C_{ant} (µmol kg^{-1})
C_{nat} (µmol kg^{-1})
2009
2016
Ocean Data View / DIVA

Fig. 4

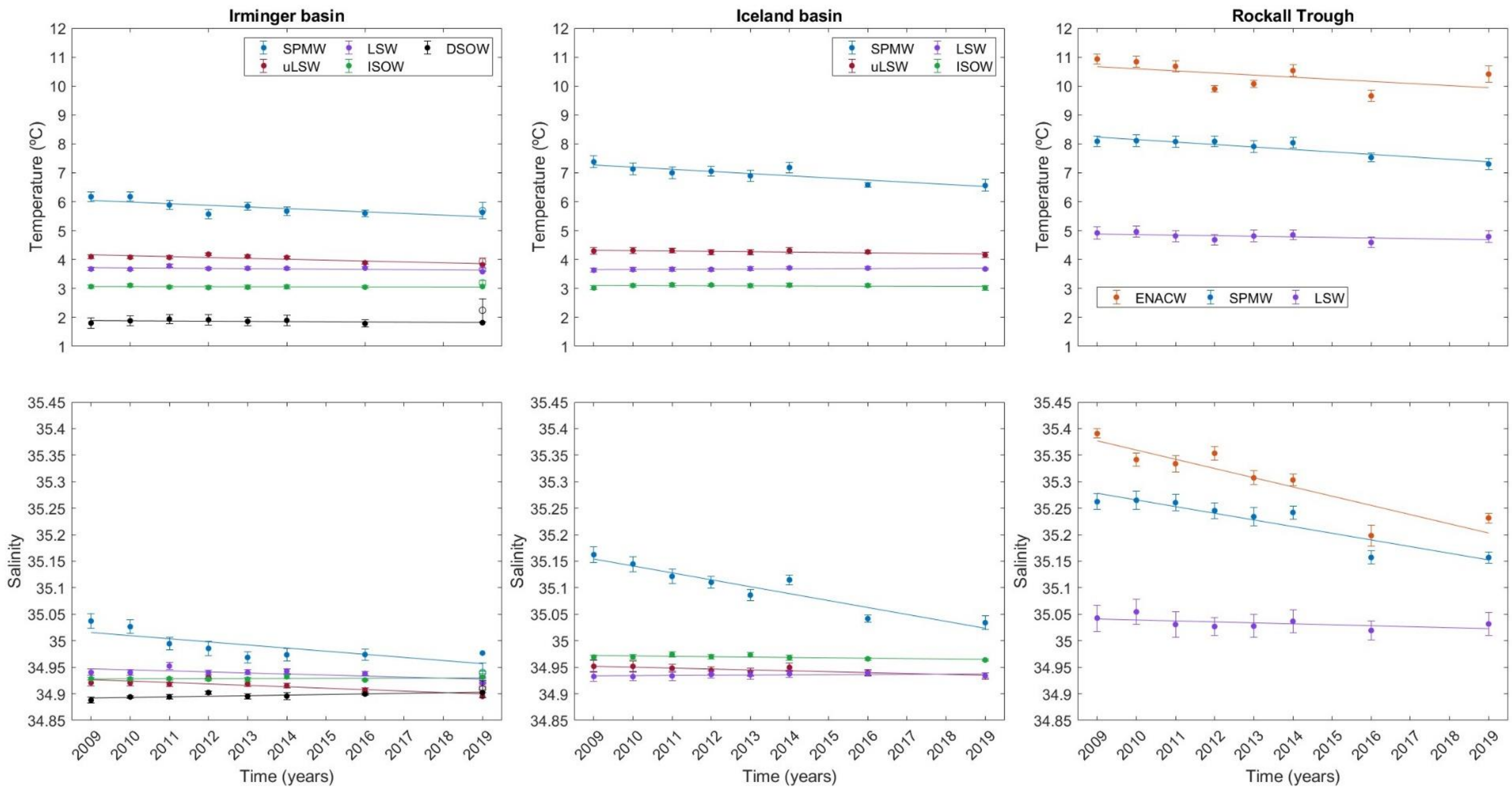

Irminger basin
Iceland basin
Rockall Trough
SPMW
LSW
DSOW
uLSW
ISOW
ENACW
Temperature (ºC)
Salinity
Time (years)

Fig. 5

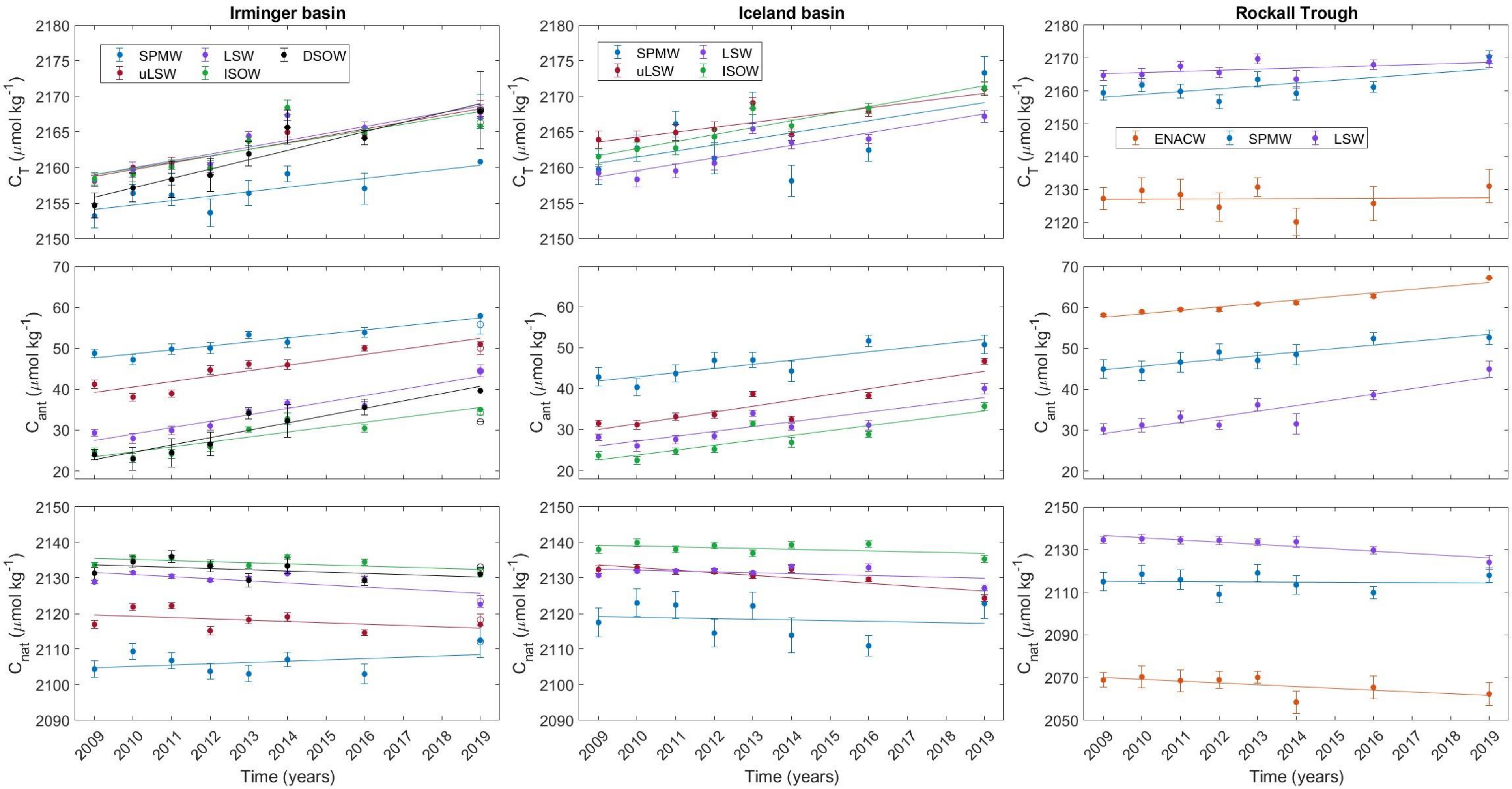

Irminger basin
Iceland basin
Rockall Trough
SPMW
uLSW
LSW
ISOW
DSOW
ENACW
C_T (μmol kg^{-1})
C_{ant} (μmol kg^{-1})
C_{nat} (μmol kg^{-1})
Time (years)

Fig. 6

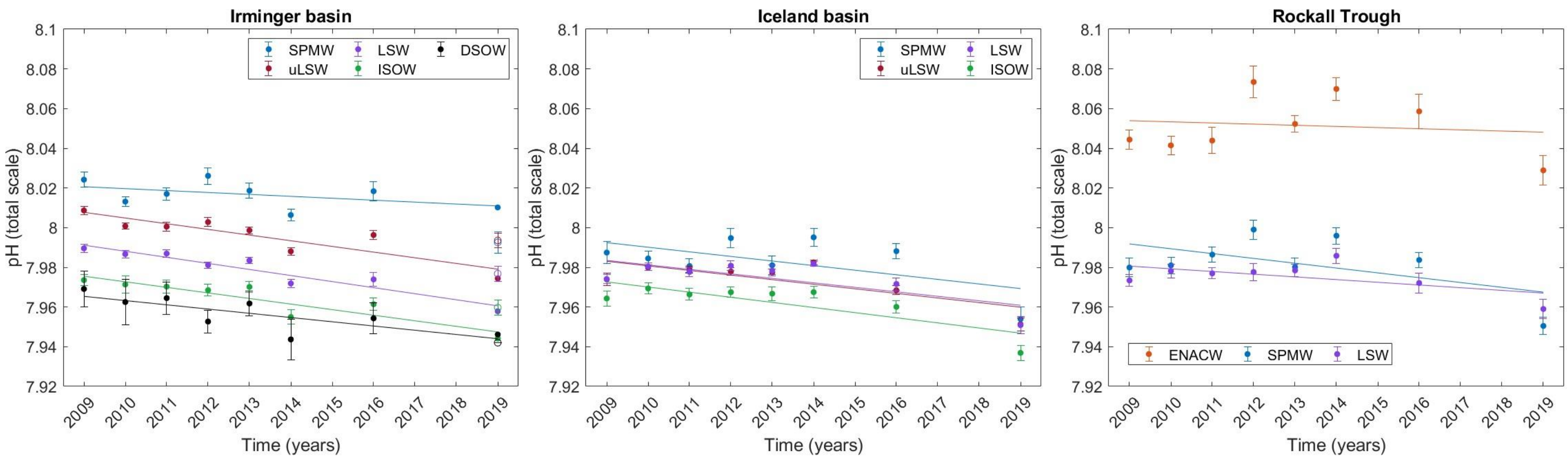

Irminger basin
SPMW
uLSW
LSW
ISOW
DSOW
Iceland basin
SPMW
uLSW
LSW
ISOW
Rockall Trough
ENACW
SPMW
LSW
pH (total scale)
Time (years)

Fig. 7

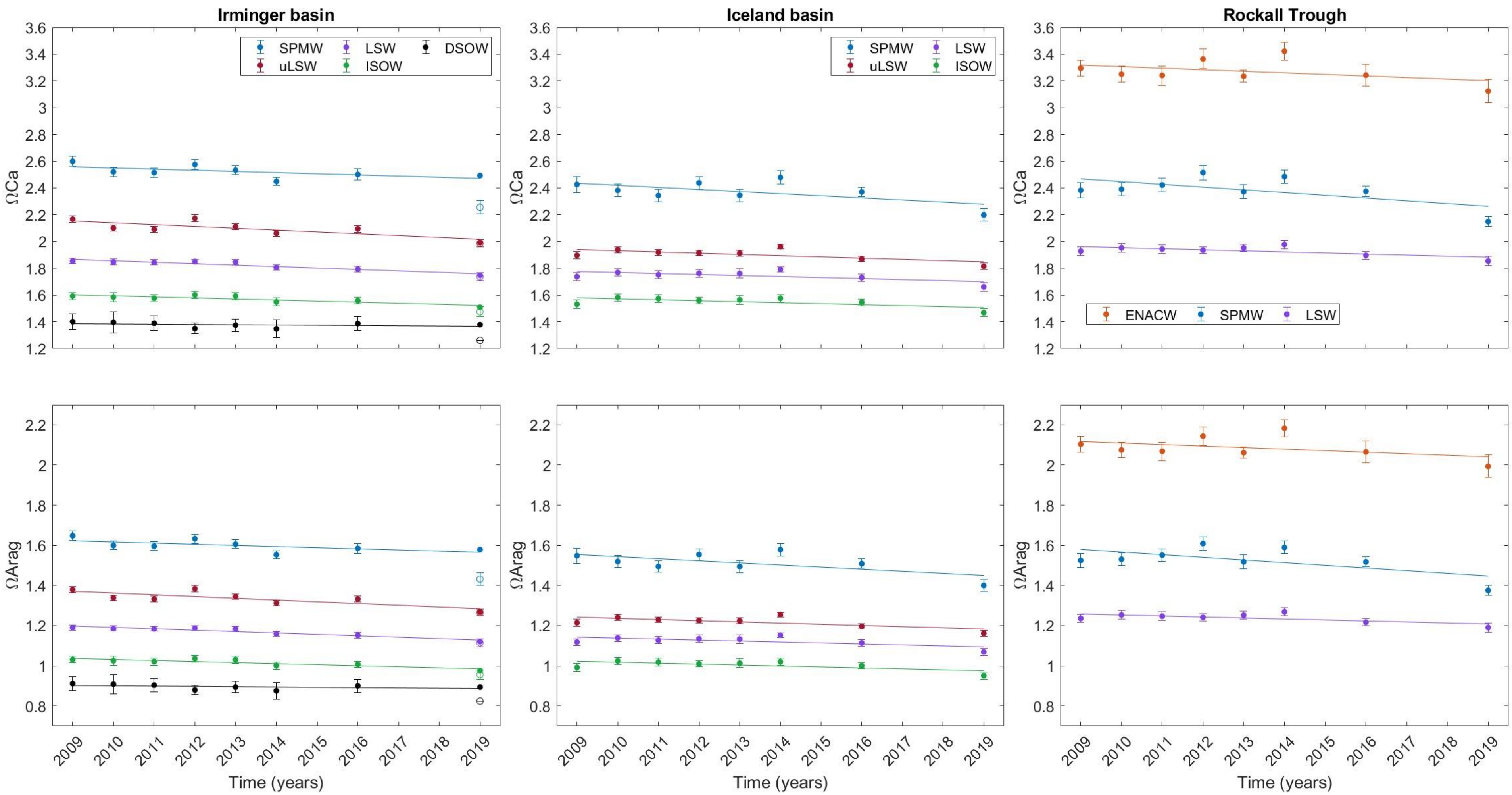
Irminger basin
Iceland basin
Rockall Trough
SPMW
uLSW
LSW
ISOW
DSOW
ENACW
ΩCa
ΩArag
Time (years)

Table 1

Year	Cruise ID	Date	Research Vessel (R/V)	Chief Scientist	Number of stations	MCS measured variables
2009	AI28	Aug 15-Sept 27	Akademik Ioffe	A. Sokov	67	A_T, C_T and pH
2010	AI31	Sep 2-Sep 27	Akademik Ioffe	A. Sokov	84	A_T, C_T and pH
2011	SV33	Sep 9-Sep 28	Akademik Sergey Vavilov	A. Sokov	98	A_T, C_T and pH
2012	AI38	May 25-Jul 1	Akademik Ioffe	S. Gladyshev	66	A_T, C_T and pH
2013	AI41	Jun 26-Jul 23	Akademik Ioffe	S. Gladyshev	75	A_T, C_T and pH
2014	AI44	Jun 27-Jul 20	Akademik Ioffe	S. Gladyshev	76	A_T, C_T and pH
2016	AI51	Jun 3-Jul 13	Akademik Ioffe	S. Gladyshev	104	A_T, C_T and pH
2019	AMK77	Aug 8-Sep 10	Akademik Mstislav Keldysh	S. Gladyshev	47	A_T and C_T

Table 2

Basin	Layer	Temperature			Salinity			C_T			C_{ant}			C_{nat}			pH_T			Ώca			ΏArag		
		ratio (ºC yr^{-1})	r^2	p-value	ratio (psu yr^{-1})	r^2	p-value	ratio (µmol kg^{-1} yr^{-1})	r^2	p-value	ratio (µmol kg^{-1} yr^{-1})	r^2	p-value	ratio (µmol kg^{-1} yr^{-1})	r^2	p-value	ratio (10^{-3} units yr^{-1})	r^2	p-value	ratio (units yr^{-1})	r^2	p-value	ratio (units yr^{-1})	r^2	p-value
Irminger	**SPMW**	**-0.058 ± 0.024**	0.60	0.02	**-0.006 ± 0.003**	0.59	0.03	**0.62 ± 0.23**	0.66	0.02	**0.95 ± 0.17**	0.89	<0.01	**-1.00 ± 0.42**	0.60	0.02	-1.25 ± 0.93	0.32	0.14	**-0.011 ± 0.006**	0.50	0.05	**-0.007 ± 0.003**	0.53	0.04
	uLSW	-0.014 ± 0.011	0.30	0.16	**-0.002 ± 0.001**	0.59	0.03	**1.02 ± 0.18**	0.89	<0.01	**1.48 ± 0.29**	0.87	<0.01	-0.47 ± 0.38	0.28	0.18	**-2.62 ± 0.69**	0.79	<0.01	-0.008 ± 0.005	0.40	0.09	-0.006 ± 0.003	0.44	0.08
	LSW	-0.010 ± 0.008	0.31	0.15	**-0.002 ± 0.001**	0.50	0.05	**0.98 ± 0.26**	0.78	<0.01	**1.53 ± 0.23**	0.92	<0.01	-0.54 ± 0.30	0.46	0.06	**-3.17 ± 0.52**	0.91	<0.01	**-0.014 ± 0.003**	0.85	<0.01	**-0.009 ± 0.002**	0.85	<0.01
	ISOW	-0.002 ± 0.003	0.11	0.42	0.000 ± 0.000	0.00	0.99	**0.90 ± 0.34**	0.64	0.02	**1.18 ± 0.29**	0.81	<0.01	-0.27 ± 0.20	0.32	0.14	**-2.97 ± 0.70**	0.83	<0.01	**-0.010 ± 0.003**	0.73	<0.01	**-0.007 ± 0.002**	0.74	<0.01
	DSOW	-0.008 ± 0.008	0.22	0.25	0.001 ± 0.001	0.43	0.08	**1.32 ± 0.23**	0.90	<0.01	**1.77 ± 0.32**	0.89	<0.01	-0.32 ± 0.33	0.19	0.28	**-2.41 ± 0.87**	0.67	<0.01	-0.004 ± 0.003	0.39	0.10	-0.003 ± 0.002	0.46	0.07
Iceland	**SPMW**	**-0.074 ± 0.022**	0.74	<0.01	**-0.013 ± 0.002**	0.89	<0.01	0.85 ± 0.64	0.32	0.15	**1.02 ± 0.31**	0.74	<0.01	-0.19 ± 0.74	0.02	0.75	-2.32 ± 1.63	0.34	0.13	-0.016 ± 0.010	0.37	0.11	-0.010 ± 0.007	0.39	0.10
	uLSW	**-0.012 ± 0.005**	0.63	0.02	**-0.002 ± 0.000**	0.76	<0.01	**0.68 ± 0.22**	0.71	<0.01	**1.42 ± 0.38**	0.78	<0.01	**-0.74 ± 0.21**	0.75	<0.01	**-2.31 ± 1.01**	0.58	0.03	-0.009 ± 0.005	0.46	0.07	-0.006 ± 0.003	0.47	0.06
	LSW	0.005 ± 0.003	0.43	0.08	0.000 ± 0.000	0.28	0.18	**0.88 ± 0.22**	0.80	<0.01	**1.18 ± 0.35**	0.75	<0.01	-0.26 ± 0.26	0.20	0.27	**-2.26 ± 1.06**	0.54	0.04	-0.008 ± 0.005	0.41	0.09	-0.005 ± 0.003	0.41	0.09
	ISOW	-0.003 ± 0.006	0.05	0.61	**-0.001 ± 0.000**	0.47	0.05	**0.98 ± 0.17**	0.89	<0.01	**1.20 ± 0.32**	0.79	<0.01	-0.23 ± 0.21	0.23	0.23	**-2.58 ± 0.99**	0.64	<0.01	-0.007 ± 0.004	0.42	0.08	-0.005 ± 0.003	0.43	0.08
Rockall	**ENACW**	-0.073 ± 0.061	0.27	0.19	**-0.017 ± 0.004**	0.80	<0.01	0.05 ± 0.57	0.00	0.92	**0.85 ± 0.11**	0.94	<0.01	-0.84 ± 0.50	0.43	0.08	-0.58 ± 2.31	0.02	0.77	-0.012 ± 0.013	0.18	0.30	-0.008 ± 0.008	0.19	0.28
	SPMW	**-0.085 ± 0.019**	0.84	<0.01	**-0.013 ± 0.003**	0.85	<0.01	**0.86 ± 0.46**	0.48	0.05	**0.87 ± 0.18**	0.86	<0.01	-0.07 ± 0.59	0.00	0.88	-2.43 ± 1.90	0.30	0.16	-0.021 ± 0.013	0.38	0.10	-0.013 ± 0.008	0.39	0.10
	LSW	-0.020 ± 0.016	0.29	0.17	-0.002 ± 0.001	0.30	0.16	0.35 ± 0.29	0.27	0.19	**1.38 ± 0.34**	0.81	<0.01	**-1.05 ± 0.24**	0.84	<0.01	-1.36 ± 0.97	0.34	0.13	-0.008 ± 0.004	0.45	0.07	-0.005 ± 0.003	0.45	0.07

Table 3

Basin	Layer	$\frac{\partial pH_T}{\partial T}\frac{\partial T}{dt}$			$\frac{\partial pH_T}{\partial S}\frac{\partial S}{dt}$			$\frac{\partial pH_T}{\partial A_T}\frac{\partial NA_T}{dt}$			$\frac{\partial pH_T}{\partial C_T}\frac{\partial NC_T}{dt}$			$\frac{dpH_T}{dt}\ (obs)$			$\frac{dpH_T}{dt}\ (calculated)$		
Irminger	SPMW	0.91	±	0.38	0.05	±	0.02	0.31	±	0.43	-2.67	±	0.63	-1.25	±	0.93	-1.41	±	0.85
	uLSW	0.22	±	0.17	0.02	±	0.01	-0.10	±	0.40	-2.99	±	0.53	-2.62	±	0.69	-2.86	±	0.68
	LSW	0.16	±	0.12	0.01	±	0.01	-0.04	±	0.39	-2.85	±	0.62	-3.17	±	0.52	-2.72	±	0.74
	ISOW	0.03	±	0.05	0.00	±	0.00	-0.13	±	0.30	-2.38	±	0.88	-2.97	±	0.70	-2.48	±	0.93
	DSOW	0.13	±	0.12	-0.01	±	0.00	-0.60	±	0.18	-3.41	±	0.62	-2.41	±	0.87	-3.90	±	0.66
Iceland	SPMW	1.15	±	0.35	0.10	±	0.02	0.61	±	0.19	-4.14	±	1.76	-2.32	±	1.63	-2.27	±	1.81
	uLSW	0.19	±	0.08	0.01	±	0.00	-0.24	±	0.45	-2.08	±	0.66	-2.31	±	1.01	-2.12	±	0.80
	LSW	-0.08	±	0.05	0.00	±	0.00	-0.04	±	0.44	-2.26	±	0.57	-2.26	±	1.06	-2.38	±	0.72
	ISOW	0.04	±	0.10	0.01	±	0.00	0.12	±	0.40	-2.70	±	0.43	-2.58	±	0.99	-2.53	±	0.60
Rockall	ENACW	1.13	±	0.94	0.14	±	0.04	0.73	±	0.66	-2.25	±	1.39	-0.58	±	2.31	-0.25	±	1.80
	SPMW	1.31	±	0.29	0.10	±	0.02	0.47	±	0.22	-3.84	±	1.23	-2.43	±	1.90	-1.96	±	1.28
	LSW	0.30	±	0.24	0.01	±	0.01	-0.14	±	0.37	-0.94	±	0.86	-1.36	±	0.97	-0.76	±	0.96

Table 4

Basin	Layer		$\frac{\partial\Omega}{\partial T}\frac{\partial T}{dt}$	$\frac{\partial\Omega}{\partial S}\frac{\partial S}{dt}$	$\frac{\partial\Omega}{\partial A_T}\frac{\partial NA_T}{dt}$	$\frac{\partial\Omega}{\partial C_T}\frac{\partial NC_T}{dt}$	$\frac{d\Omega}{dt}$ (obs)	$\frac{d\Omega}{dt}$ $(calculated)$
Irminger	SPMW	Calcite	-0.57 ± 0.24	-0.43 ± 0.18	1.68 ± 2.37	-13.35 ± 3.14	-11.03 ± 5.57	-12.67 ± 3.94
		Aragonite	-0.49 ± 0.20	-0.29 ± 0.12	1.07 ± 1.50	-8.47 ± 1.99	-7.17 ± 3.46	-8.17 ± 2.50
	uLSW	Calcite	-0.17 ± 0.13	-0.12 ± 0.05	-0.46 ± 1.82	-12.61 ± 2.24	-8.28 ± 5.16	-13.36 ± 2.89
		Aragonite	-0.13 ± 0.10	-0.08 ± 0.03	-0.29 ± 1.16	-8.03 ± 1.43	-5.55 ± 3.21	-8.53 ± 1.84
	LSW	Calcite	-0.15 ± 0.11	-0.09 ± 0.05	-0.17 ± 1.55	-10.42 ± 2.27	-13.54 ± 2.88	-10.83 ± 2.75
		Aragonite	-0.11 ± 0.08	-0.06 ± 0.03	-0.11 ± 0.99	-6.69 ± 1.45	-8.65 ± 1.83	-6.97 ± 1.76
	ISOW	Calcite	-0.04 ± 0.05	0.00 ± 0.01	-0.44 ± 1.03	-7.48 ± 2.75	-10.35 ± 3.23	-7.96 ± 2.94
		Aragonite	-0.02 ± 0.04	0.00 ± 0.01	-0.29 ± 0.67	-4.84 ± 1.78	-6.66 ± 2.04	-5.15 ± 1.90
	DSOW	Calcite	-0.13 ± 0.12	0.03 ± 0.02	-1.78 ± 0.52	-9.23 ± 1.68	-4.30 ± 2.76	-11.11 ± 1.77
		Aragonite	-0.09 ± 0.09	0.02 ± 0.01	-1.16 ± 0.34	-6.01 ± 1.10	-3.02 ± 1.68	-7.24 ± 1.15
Iceland	SPMW	Calcite	-0.88 ± 0.26	-0.86 ± 0.16	3.16 ± 1.00	-19.59 ± 8.35	-15.77 ± 10.40	-18.17 ± 8.42
		Aragonite	-0.72 ± 0.22	-0.58 ± 0.10	2.02 ± 0.64	-12.48 ± 5.32	-10.37 ± 6.55	-11.77 ± 5.37
	uLSW	Calcite	-0.17 ± 0.07	-0.09 ± 0.03	-1.02 ± 1.89	-7.98 ± 2.52	-9.18 ± 5.11	-9.26 ± 3.15
		Aragonite	-0.12 ± 0.05	-0.06 ± 0.02	-0.65 ± 1.21	-5.11 ± 1.61	-5.92 ± 3.23	-5.95 ± 2.02
	LSW	Calcite	0.08 ± 0.05	0.02 ± 0.01	-0.15 ± 1.70	-7.92 ± 2.00	-7.53 ± 4.64	-7.97 ± 2.63
		Aragonite	0.06 ± 0.03	0.01 ± 0.01	-0.09 ± 1.09	-5.10 ± 1.29	-4.83 ± 2.96	-5.12 ± 1.69
	ISOW	Calcite	-0.04 ± 0.10	-0.03 ± 0.02	0.41 ± 1.37	-8.38 ± 1.33	-7.22 ± 4.34	-8.05 ± 1.91
		Aragonite	-0.03 ± 0.07	-0.02 ± 0.01	0.27 ± 0.89	-5.43 ± 0.86	-4.72 ± 2.76	-5.22 ± 1.24
Rockall	ENACW	Calcite	-0.82 ± 0.69	-1.50 ± 0.38	5.16 ± 4.63	-14.21 ± 8.78	-11.60 ± 12.67	-11.37 ± 9.95
		Aragonite	-0.79 ± 0.66	-1.00 ± 0.25	3.29 ± 2.95	-9.06 ± 5.60	-7.66 ± 7.96	-7.57 ± 6.37
	SPMW	Calcite	-1.15 ± 0.26	-0.82 ± 0.18	2.44 ± 1.15	-18.21 ± 5.83	-20.57 ± 13.40	-17.74 ± 5.95
		Aragonite	-0.93 ± 0.21	-0.55 ± 0.12	1.56 ± 0.74	-11.66 ± 3.73	-13.24 ± 8.47	-11.58 ± 3.81
	LSW	Calcite	-0.28 ± 0.22	-0.10 ± 0.08	-0.58 ± 1.57	-3.62 ± 3.30	-7.88 ± 4.41	-4.59 ± 3.66
		Aragonite	-0.21 ± 0.16	-0.07 ± 0.05	-0.37 ± 1.01	-2.33 ± 2.12	-4.97 ± 2.82	-2.97 ± 2.35

References

Accornero, A., Manno, C., Esposito, F., & Gambi, M.C. (2003). The vertical flux of particulate matter in the polynya of Terra Nova Bay. Part II. Biological components. Antarctic Science, 15, 175–188. DOI: 10.1017/S0954102003001214

Álvarez, M., Pérez, F.F., Bryden, H., & Ríos, A.F. (2004). Physical and biogeochemical transports structure in the North Atlantic subpolar gyre. Journal of Geophysical Research: Ocean, 109. DOI: 10.1029/2003jc002015

Álvarez, M., Ríos, A.F., Pérez, F.F., Bryden, H.L., & Rosón, G. (2003). Transports and budgets of total inorganic carbon in the subpolar and temperate North Atlantic. Global Biogeochemical Cycles, 17(2), 2-1-2–21. DOI: 10.1029/2002gb001881

Anderson, L.G. (2001). of the Surface Ocean CO2 System in the Nordic Seas and Northern North Atlantic to Climate Change Using mixed-layer salinity and temperature Model and empirical relationships between sea surface temperature and surface water CO2 fugacity, and between sea.

Azetsu-Scott, K., Jones, E. P., Yashayaev, I., & Gershey, R. M. (2003). Time series study of CFC concentrations in the Labrador Sea during deep and shallow convection regimes (1991–2000). Journal of Geophysical Research: Oceans, 108(C11).

Balmaseda, M.A., Smith, G.C., Haines, K., Anderson, D., Palmer, T.N., & Vidard, A. (2007). Historical reconstruction of the Atlantic Meridional Overturning Circulation from the ECMWF operational ocean reanalysis. Geophysical Research Letters, 34, 1–6. DOI: 10.1029/2007GL031645

Bates, N.R., Astor, Y.M., Church, M.J., Currie, K., Dore, J.E., González-Dávila, M., Lorenzoni, L., Muller-Karger, F., Olafsson, J., & Santana-Casiano, J.M. (2014). A time-series view of changing surface ocean chemistry due to ocean uptake of anthropogenic CO2 and ocean acidification. Oceanography, 27, 126–141. DOI: 10.5670/oceanog.2014.16

Bates, N.R., Best, M.H.P., Neely, K., Garley, R., Dickson, A.G., & Johnson, R.J. (2012). Detecting anthropogenic carbon dioxide uptake and ocean acidification in the North Atlantic Ocean. Biogeosciences, 9, 2509–2522. DOI: 10.5194/bg-9-2509-2012

Bathmann, U. V., Noji, T.T., & von Bodungen, B. (1991). Sedimentation of pteropods in the Norwegian Sea in autumn. Deep Sea Research Part A. Oceanographic Research Papers, 38, 1341–1360. DOI: 10.1016/0198-0149(91)90031-A

Benson, B.B., & Krause, D. (1984). The concentration and isotopic fractionation of oxygen dissolved in freshwater and seawater in equilibrium with the atmosphere. Deep Sea Research Part B. Oceanographic Literature Review, 31, 859. DOI: 10.1016/0198-0254(84)93289-8

Bersch, M., Yashayaev, I., & Koltermann, K. P. (2007). Recent changes of the thermohaline circulation in the subpolar North Atlantic. Ocean Dynamics, 57, 223-235.

Bittig, H.C., Steinhoff, T., Claustre, H., Fiedler, B., Williams, N.L., Sauzède, R., Körtzinger, A., & Gattuso, J.P. (2018). An alternative to static climatologies: Robust estimation of open ocean CO2 variables and nutrient concentrations from T, S, and O2 data using Bayesian neural networks. Frontiers in Marine Science, 5, 1–29. DOI: 10.3389/fmars.2018.00328

Böning, C.W., Scheinert, M., Dengg, J., Biastoch, A., & Funk, A. (2006). Decadal variability of subpolar gyre transport and its reverberation in the North Atlantic overturning. Geophysical Research Letters, 33. DOI: 10.1029/2006GL026906

Brambilla, E., & Talley, L.D. (2008). Subpolar mode water in the northeastern Atlantic: 1. Averaged properties and mean circulation. Journal of Geophysical Research: Ocean, 113, 1–18. DOI: 10.1029/2006JC004062

Broecker, W.S., & Peng, T.H. (1983). Tracers in the sea: W. S. Broecker and T. H. Peng. Eldigio Press Lamont Doherty Geological Observatory, 1982, 690 pages (300 figures and tables; 740 commented bibliographic references), US $35.00. Geochimica et Cosmochimica Acta, 47, 1336. DOI: 10.1016/0016-7037(83)90075-3

Bryden, H.L., King, B.A., Mccarthy, G.D., & Mcdonagh, E.L. (2014). Impact of a 30 % reduction in Atlantic meridional overturning during 2009 – 2010 683–691. DOI: 10.5194/os-10-683-2014

Caldeira, K., & Wickett, M. (2005). Ocean model predictions of chemistry changes from carbon dioxide emissions to the atmosphere and ocean. Journal of Geophysical Research C: Oceans, 110, 1–12. DOI: 10.1029/2004JC002671

Caldeira, K., & Wickett, M.E. (2003). Anthropogenic carbon and ocean pH. Nature, 425, 365. DOI: 10.1038/425365a

Carpenter, J. H. (1965). The accuracy of the Winkler method for dissolved oxygen analysis 1. Limnology and Oceanography, 10(1), 135-140.

Carrit, D. E., & Carpenter, J. H. (1966). Recommendation procedure for Winkler analyses of sea water for dissolved oxygen. Journal of Marine Research, 24, 313-318.

Carter, B.R., Bittig, H.C., Fassbender, A.J., Sharp, J.D., Takeshita, Y., Xu, Y.Y., Álvarez, M., Wanninkhof, R., Feely, R.A., & Barbero, L. (2021). New and updated global empirical seawater property estimation routines. Limnology and Oceanography: Methods, 19, 785–809. DOI: 10.1002/lom3.10461

Chau, T.-T.-T., Gehlen, M., Metzl, N., and Chevallier, F.: CMEMS-LSCE: a global, 0.25°, monthly reconstruction of the surface ocean carbonate system, Earth Syst. Sci. Data, 16, 121–160, https://doi.org/10.5194/essd-16-121-2024, 2024.

Clayton, T.D., & Byrne, R.H. (1993). Spectrophotometric seawater pH measurements: total hydrogen ion concentration scale calibration of m-cresol purple and at-sea results. Deep

Sea Research Part I: Oceanographic Research Papers, 40, 2115–2129. DOI: 10.1016/0967-0637(93)90048-8

Collier, R., Dymond, J., Honjo, S., Manganini, S., Francois, R., & Dunbar, R. (2000). The vertical flux of biogenic and lithogenic material in the Ross Sea: Moored sediment trap observations 1996-1998. Deep Sea Research Part II: Topical Studies in Oceanography, 47, 3491–3520. DOI: 10.1016/S0967-0645(00)00076-X

Corbière, A., Metzl, N., Reverdin, G., Brunet, C., & Takahashi, T. (2007). Interannual and decadal variability of the oceanic carbon sink in the North Atlantic subpolar gyre. Tellus, Series B: Chemical and Physical Meteorology, 59, 168–178. DOI: 10.1111/j.1600-0889.2006.00232.x

Daniault, N., Mercier, H., Lherminier, P., Sarafanov, A., Falina, A., Zunino, P., Pérez, F.F., & Ríos, A.F. (2016). The northern North Atlantic Ocean mean circulation in the early 21st century. Progress in Oceanography, 146, 142–158. DOI: 10.1016/j.pocean.2016.06.007

de la Paz, M., García-Ibáñez, M. I., Steinfeldt, R., Ríos, A. F., & Pérez, F. F. (2017). Ventilation versus biology: What is the controlling mechanism of nitrous oxide distribution in the North Atlantic?. Global Biogeochemical Cycles, 31(4), 745–760. DOI: 10.1002/2016GB005507

Dickson, A. D. 1995. Determination of dissolved oxygen in sea water by Winkler titration. WOCE Operations Manual, Part 3.1.3 Operations & Methods, WHP Office Report WHPO 91-1.

Dickson, A. G., & Goyet, C. (1994). Handbook of methods for the analysis of the various parameters of the carbon dioxide system in sea water. V. 2. United States. DOI: 10.2172/10107773

Dickson, A. G., Sabine, C. L., & Christian, J. R. (2007). Guide to best practices for ocean CO2 measurements. PICES Special Publication 3, 191 pp.

Dickson, B., Yashayaev, I., Meincke, J., Turrell, B., Dye, S., & Holfort, J. (2002). Rapid freshening of the deep North Atlantic Ocean over the past four decades. Nature, 416(6883), 832-837. DOI: 10.1038/416832a

De Jong, M. F., & de Steur, L. (2016). Strong winter cooling over the Irminger Sea in winter 2014–2015, exceptional deep convection, and the emergence of anomalously low SST. Geophysical Research Letters, 43, 7106–7113. DOI: 10.1002/2016GL069596

De Jong, M. F., Van Aken, H. M., Våge, K., & Pickart, R. S. (2012). Convective mixing in the central Irminger Sea: 2002-2010. Deep Sea Research Part I: Oceanographic Research Papers, 63, 36–51. DOI: 10.1016/j.dsr.2012.01.003

DelValls, T. A., & Dickson, A. G. (1998). The pH of buffers based on 2-amino-2-hydroxymethyl-1,3-propanediol ('tris') in synthetic sea water. Deep Sea Research Part I: Oceanographic Research Papers, 45, 1541–1554. DOI: 10.1016/S0967-0637(98)00019-3

Desbruyères, D., Thierry, V., & Mercier, H. (2013). Simulated decadal variability of the meridional overturning circulation across the A25-Ovide section, 462–475. DOI: 10.1029/2012JC008342

Dickson, A. G. (1990). Standard potential of the reaction: AgCl(s) + 1/2H2(g) = Ag(s) + HCl(aq), and the standard acidity constant of the ion HSO4- in synthetic sea water from 273.15 to 318.15 K. J. Chem. Thermodyn., 22, 113–127. DOI: 10.1016/0021-9614(90)90074-Z

Dickson, A. G., & Millero, F. J. (1987). A comparison of the equilibrium constants for the dissociation of carbonic acid in seawater media. Deep Sea Research Part A: Oceanographic Research Papers, 34, 1733–1743. DOI: 10.1016/0198-0149(87)90021-5

Dickson, R. R., & Brown, J. (1994). The production of North Atlantic Deep Water: Sources, rates, and pathways. J. Geophys. Res. Ocean., 99, 12319–12341. DOI: 10.1029/94JC00530

Doney, S. C., Fabry, V. J., Feely, R. A., & Kleypas, J. A. (2009). Ocean Acidification: The Other CO2 Problem. Ann. Rev. Mar. Sci., 1, 169–192. DOI: 10.1146/annurev.marine.010908.163834

Eden, C., & Willebrand, J. (2001). Mechanism of interannual to decadal variability of the North Atlantic circulation. J. Clim., 14, 2266–2280. DOI: 10.1175/1520-0442(2001)014<2266:MOITDV>2.0.CO;2

Ellett, D. J., Edwards, A., & Bowers, R. (1986). The hydrography of the Rockall Channel—an overview. Proc. R. Soc. Edinburgh. Sect. B. Biol. Sci., 88, 61–81. DOI: 10.1017/s0269727000004474

Feely, R. A., Sabine, C. L., Lee, K., Berelson, W., Kleypas, J., Fabry, V. J., Millero, F. J. (2004). Impact of anthropogenic CO2 on the CaCO3 system in the oceans. Science, 305, 362–366. DOI: 10.1126/SCIENCE.1097329

Ferron, B., Kokoszka, F., Mercier, H., Lherminier, P. (2014). Dissipation rate estimates from microstructure and finescale internal wave observations along the A25 Greenland-Portugal OVIDE line. J. Atmos. Ocean. Technol., 31, 2530–2543. DOI: 10.1175/JTECH-D-14-00036.1

Fogelqvist, E., Blindheim, J., Tanhua, T., Østerhus, S., Buch, E., & Rey, F. (2003). Greenland–Scotland overflow studied by hydro-chemical multivariate analysis. Deep Sea Research Part I: Oceanographic Research Papers, 50(1), 73-102.

Fontela, M., Pérez, F. F., Carracedo, L. I., Padín, X. A., Velo, A., García-Ibañez, M. I., Lherminier, P. (2020). The Northeast Atlantic is running out of excess carbonate in the horizon of cold-water corals communities. Sci. Rep., 10. DOI: 10.1038/s41598-020-71793-2

Friedlingstein, P., Sullivan, M. O., Jones, M. W., Andrew, R. M., Gregor, L., Hauck, J., Quéré, C. Le, Luijkx, I. T., Olsen, A., Peters, G. P., Peters, W. (2022). Global Carbon Budget 2022, 4811–4900.

Fröb, F., Olsen, A., Becker, M., Chafik, L., Johannessen, T., Reverdin, G., Omar, A. (2019). Wintertime fCO2 Variability in the Subpolar North Atlantic Since 2004. Geophys. Res. Lett., 46, 1580–1590. DOI: 10.1029/2018GL080554

Fröb, F., Olsen, A., Våge, K., Moore, G. W. K., Yashayaev, I., Jeansson, E., Rajasakaren, B. (2016). Irminger Sea deep convection injects oxygen and anthropogenic carbon to the ocean interior. Nat. Commun., 7. DOI: 10.1038/ncomms13244

García-Ibáñez, M. I., Bates, N. R., Bakker, D. C. E., Fontela, M., Velo, A. (2021). Cold-water corals in the Subpolar North Atlantic Ocean exposed to aragonite undersaturation if the 2 °C global warming target is not met. Global Planetary Change, 201. DOI: 10.1016/j.gloplacha.2021.103480

García-Ibáñez, M. I., Pardo, P. C., Carracedo, L. I., Mercier, H., Lherminier, P., Ríos, A. F., Pérez, F. F. (2015). Structure, transports and transformations of the water masses in the Atlantic Subpolar Gyre. Progress in Oceanography, 135, 18-36. DOI: 10.1016/j.pocean.2015.03.009

García-Ibáñez, M. I., Pérez, F. F., Lherminier, P., Zunino, P., Mercier, H., Tréguer, P. (2018). Water mass distributions and transports for the 2014 GEOVIDE cruise in the North Atlantic. Biogeosciences, 15, 2075-2090. DOI: 10.5194/bg-15-2075-2018

García-Ibáñez, M. I., Zunino, P., Fröb, F., Carracedo, L. I., Ríos, A. F., Mercier, H., Olsen, A., Pérez, F. F. (2016). Ocean acidification in the subpolar North Atlantic: Rates and mechanisms controlling pH changes. Biogeosciences, 13, 3701-3715. DOI: 10.5194/bg-13-3701-2016

Gehlen, M., Séférian, R., Jones, D. O. B., Roy, T., Roth, R., Barry, J., Bopp, L., Doney, S. C., Dunne, J. P., Heinze, C., Joos, F., Orr, J. C., Resplandy, L., Segschneider, J., and Tjiputra, J.: Projected pH reductions by 2100 might put deep North Atlantic biodiversity at risk, Biogeosciences, 11, 6955-6967, 10.5194/bg-11-6955-2014, 2014.

Gladyshev, S. V., Gladyshev, V. S., Falina, A. S., Sarafanov, A. A. (2016a). Winter convection in the Irminger Sea in 2004–2014. Oceanology, 56, 326-335. DOI: 10.1134/S0001437016030073

Gladyshev, S. V., Gladyshev, V. S., Gulev, S. K., Sokov, A. V. (2016b). Anomalously deep convection in the Irminger Sea during the winter of 2014–2015. Doklady Earth Sciences, 469, 766-770. DOI: 10.1134/S1028334X16070229

Gladyshev, S. V., Gladyshev, V. S., Member, C., Gulev, R. A. S. S. K., Sokov, A. V. (2018). Structure and Variability of the Meridional Overturning Circulation in the North Atlantic Subpolar Gyre, 2007–2017. Doklady Earth Sciences, 483, 1524-1527. DOI: 10.1134/S1028334X18120024

Gladyshev, S. V., Gladyshev, V. S., Member, C., Gulev, R. A. S. S. K., Sokov, A. V. (2017). Subpolar Mode Water Classes in the Northeast Atlantic: Interannual and Long-Term Variability. Doklady Earth Sciences, 476, 1203-1206. DOI: 10.1134/S1028334X17100166

González-Dávila, M., & Santana-Casiano, J. M. (2023). Long-term trends of pH and inorganic carbon in the Eastern North Atlantic: the ESTOC site. *Frontiers in Marine Science*, *10*, 1236214.

González-Dávila, M., Santana-Casiano, J. M., Petihakis, G., Ntoumas, M., Suárez de Tangil, M., Krasakopoulou, E. (2016). Seasonal pH variability in the Saronikos Gulf: A year-study using a new photometric pH sensor. Journal of Marine Systems, 162, 37-46. DOI: 10.1016/j.jmarsys.2016.03.007

González-Dávila, M., Santana-Casiano, J. M., Prêcheur-Massieu, H. (2014). New pH sensor for monitoring ocean acidification. Sea Technology, 55, 36-40.

González-Dávila, M., Santana-Casiano, J.M., Rueda, M.J., Llinás, O. (2010). The water column distribution of carbonate system variables at the ESTOC site from 1995 to 2004. Biogeosciences, 7, 3067-3081. DOI: 10.5194/bg-7-3067-2010

Gruber, N., Clement, D., Carter, B.R., Feely, R.A., van Heuven, S., Hoppema, M., Ishii, M., Key, R.M., Kozyr, A., Lauvset, S.K., Monaco, C. Lo, Mathis, J.T., Murata, A., Olsen, A., Perez, F.F., Sabine, C.L., Tanhua, T., Wanninkhof, R. (2019a). The oceanic sink for anthropogenic CO2 from 1994 to 2007. Science, 363, 1193

Gruber, N., Sarmiento, J.L., Stocker, T.F. (1996). An improved method for detecting anthropogenic CO2 in the oceans. Global Biogeochem. Cycles. https://doi.org/10.1029/96GB01608

Guallart, E.F., Fajar, N.M., Padín, X.A., Vázquez-Rodríguez, M., Calvo, E., Ríos, A.F., Hernández-Guerra, A., Pelejero, C., Pérez, F.F. (2015). Ocean acidification along the 24.5°N section in the subtropical North Atlantic. Geophys. Res. Lett., 42, 450–458. https://doi.org/10.1002/2014GL062971

Häkkinen, S. (2002). Surface salinity variability in the northern North Atlantic during recent decades. J. Geophys. Res. Ocean, 107, SRF 4-1. https://doi.org/10.1029/2001JC000812

Häkkinen, S., Rhines, P.B. (2004). Decline of Subpolar North Atlantic Circulation during the 1990s. Science (80-.), 304, 555–559. https://doi.org/10.1126/science.1094917

Harvey, J. (1982). Theta–S relationships and water masses in the eastern North Atlantic. Deep-Sea Res. Part a-Oceanogr. Res. Pap., 29 (8), 1021–1033.

Hátún, H., Sande, A.B., Drange, H., Hansen, B., Valdimarsson, H. (2005). Influence of the Atlantic subpolar gyre on the thermohaline circulation. Science (80-.), 309, 1841–1844. https://doi.org/10.1126/science.1114777

Holliday, N.P., Bersch, M., Berx, B., Chafik, L., Cunningham, S., Florindo-López, C., Hátún, H., Johns, W., Josey, S.A., Larsen, K.M.H., Mulet, S., Oltmanns, M., Reverdin, G., Rossby, T., Thierry, V., Valdimarsson, H., Yashayaev, I. (2020). Ocean circulation causes the largest freshening event for 120 years in eastern subpolar North Atlantic. Nat. Commun., 11. https://doi.org/10.1038/s41467-020-14474-y

Holliday, P. N., Pollard, R.T., Read, J.F., Leach, H. (2000). Water mass properties and fluxes in the Rockall Trough, 1975-1998. Deep-Sea Research Part I: Oceanographic Research Papers. https://doi.org/10.1016/S0967-0637(99)00109-0

Humphreys, M. P., et al. (2016). Multidecadal accumulation of anthropogenic and remineralized dissolved inorganic carbon along the Extended Ellett Line in the northeast Atlantic Ocean. Global Biogeochem. Cycles. 30, 293–310, doi:10.1002/2015GB005246.

IPCC. (2013). Climate Change 2013: The Physical Science Basis. Contribution of Working Group I to the Fifth Assessment Report of the Intergovernmental Panel on Climate Change. Cambridge University Press.

IPCC. (2021). Climate Change 2021: The Physical Science Basis. Contribution of Working Group I to the Sixth Assessment Report of the Intergovernmental Panel on Climate Change. Cambridge University Press.

Jackson, L.C., Biastoch, A., Buckley, M.W., Desbruyères, D. G., Frajka-Williams, E., Moat, B., and Robson, J. (2022). The evolution of the North Atlantic Meridional Overturning Circulation since 1980. Nat. Rev. Earth Environ. 3, 241–254. https://doi.org/10.1038/s43017-022-00263-2

Jiang, L.Q., Feely, R.A., Carter, B.R., Greeley, D.J., Gledhill, D.K., Arzayus, K.M. (2015). Climatological distribution of aragonite saturation state in the global oceans. Global Biogeochem. Cycles, 29, 1656–1673. https://doi.org/10.1002/2015GB005198

Johnson, K.M., Wills, K.D., Butler, D.B., Johnson, W.K., Wong, C.S. (1993). Coulometric total carbon dioxide analysis for marine studies: maximizing the performance of an automated gas extraction system and coulometric detector. Mar. Chem., 44, 167–187. https://doi.org/10.1016/0304-4203(93)90201-X

Josey, S.A., Hirschi, J.J.M., Sinha, B., Duchez, A., Grist, J.P., Marsh, R. (2018). The recent Atlantic cold anomaly: Causes, consequences, and related phenomena. Ann. Rev. Mar. Sci., 10, 475–501. https://doi.org/10.1146/annurev-marine-121916-063102

Jung, T., Vitart, F., Ferranti, L., and Morcrette, J. J. (2011). Origin and predictability of the extreme negative NAO winter of 2009/10. Geophysical Research Letters, 38(7).

Khatiwala, S., Tanhua, T., Mikaloff Fletcher, S., Gerber, M., Doney, S.C., Graven, H.D., Gruber, N., McKinley, G.A., Murata, A., Ríos, A.F., Sabine, C.L. (2013). Global ocean storage of anthropogenic carbon. Biogeosciences, 10, 2169–2191. https://doi.org/10.5194/bg-10-2169-2013

Kieke, D., Rhein, M., Stramma, L., Smethie, W. M., Bullister, J. L., & LeBel, D. A. (2007). Changes in the pool of Labrador Sea Water in the subpolar North Atlantic. Geophysical Research Letters, 34(6).

Knight, J.R., Folland, C.K., Scaife, A.A. (2006). Climate impacts of the Atlantic multidecadal oscillation. Geophys. Res. Lett., 33, 2–5. https://doi.org/10.1029/2006GL026242

Langdon, C., Takahashi, T., Sweeney, C., Chipman, D., Atkinson, J. (2000). Rate of an experimental coral reef responds to manipulations in the concentrations of both CaCO3. Global Biogeochem. Cycles, 14, 639–654.

Lauvset, S. K., Gruber, N., Landschützer, P., Olsen, A., and Tjiputra, J.: Trends and drivers in global surface ocean pH over the past 3 decades. Biogeosciences, 12, 1285-1298, doi:10.5194/bg-12-1285-2015, 2015

Lazier, J., Hendry, R., Clarke, A., Yashayaev, I., Rhines, P. (2002). Convection and restratification in the Labrador Sea, 1990–2000. Deep Sea Res. Part I Oceanogr. Res. Pap., 49, 1819–1835. https://doi.org/10.1016/S0967-0637(02)00064-X

Lee, K., Kim, T.W., Byrne, R.H., Millero, F.J., Feely, R.A., Liu, Y.M. (2010). The universal ratio of boron to chlorinity for the North Pacific and North Atlantic oceans. Geochim. Cosmochim. Acta, 74, 1801–1811. https://doi.org/10.1016/j.gca.2009.12.027

Leseurre, C., Lo Monaco, C., Reverdin, G., Metzl, N., Fin, J., Olafsdottir, S., Racapé, V. (2020). Ocean carbonate system variability in the North Atlantic Subpolar surface water (1993–2017). Biogeosciences, 17, 2553–2577. https://doi.org/10.5194/bg-17-2553-2020

Lewis, E., Wallace, D. (1998). Program Developed for CO2 System Calculations ORNL/CDIAC-105, Carbon Dioxide Information Analysis Centre.

Lherminier, P., Mercier, H., Huck, T., Gourcuff, C., Perez, F. F., Morin, P., Sarafanov, A., and Falina, A. (2010). The Atlantic Meridional Overturning Circulation and the subpolar gyre observed at the A25-OVIDE section in June 2002 and 2004. Deep Sea Research Part I: Oceanographic Research Papers, 57(11), 1374-1391.

Lherminier, P., Perez, F. F., Branellec, P., Mercier, H., Velo, A., Messias, M. J., Castrillejo, M., Reverdin, G., Fontela, M., Baurand, F. (2022). GO-SHIP A25 - OVIDE 2018 Cruise data. SEANOE. https://doi.org/10.17882/87394

Lueker, T.J., Dickson, A.G., Keeling, C.D. (2000). Ocean pCO2 calculated from dissolved inorganic carbon, alkalinity, and equations for K1 and K2: Validation based on laboratory measurements of CO2 in gas and seawater at equilibrium. Mar. Chem., 70, 105–119. https://doi.org/10.1016/S0304-4203(00)00022-0

Marsh, R., de Cuevas, B.A., Coward, A.C., Bryden, H.L., Álvarez, M. (2005). Thermohaline circulation at three key sections in the North Atlantic over 1985–2002. Geophys. Res. Lett., 32, 1–4. https://doi.org/10.1029/2004GL022281

Matear, R.J., Lenton, A. (2014). Quantifying the impact of ocean acidification on our future climate. Biogeosciences, 11, 3965–3983. https://doi.org/10.5194/bg-11-3965-2014

Maier-Reimer, E., & Hasselmann, K. (1987). Transport and storage of CO2 in the ocean: an inorganic ocean-circulation carbon cycle model. Climate dynamics, 2, 63-90.

Maier, C., Hegeman, J., Weinbauer, M. G., & Gattuso, J. P. (2009). Calcification of the cold-water coral Lophelia pertusa, under ambient and reduced pH. Biogeosciences, 6(8), 1671-1680. https://doi.org/10.5194/bg-6-1671-2009

Mauritzen, C., Häkkinen, S. (1999). On the relationship between dense water formation and the "Meridional Overturning Cell" in the North Atlantic Ocean. Deep. Res. Part I Oceanogr. Res. Pap., 46, 877–894. https://doi.org/10.1016/S0967-0637(98)00094-6

McDonagh, E.L., King, B.A., Bryden, H.L., Courtois, P., Szuts, Z., Baringer, M., Cunningham, S.A., Atkinson, C., McCarthy, G. (2015). Continuous estimate of Atlantic oceanic freshwater flux at 26.5°N. Journal of Climate, 28, 8888–8906. https://doi.org/10.1175/JCLI-D-14-00519.1

McGrath, T., Kivimäe, C., McGovern, E., Cave, R.R., Joyce, E. (2013). Winter measurements of oceanic biogeochemical parameters in the Rockall Trough (2009-2012). Earth System Science Data, 5, 375–383. https://doi.org/10.5194/essd-5-375-2013

McGrath, T., Kivimäe, C., Tanhua, T., Cave, R.R., McGovern, E. (2012a). Inorganic carbon and pH levels in the Rockall Trough 1991-2010. Deep Sea Research Part I: Oceanographic Research Papers, 68, 79–91. https://doi.org/10.1016/j.dsr.2012.05.011

McGrath, T., Nolan, G., McGovern, E. (2012b). Chemical characteristics of water masses in the Rockall Trough. Deep Sea Research Part I: Oceanographic Research Papers, 61, 57–73. https://doi.org/10.1016/j.dsr.2011.11.007

McCartney, M. S., & Talley, L. D. (1982). The subpolar mode water of the North Atlantic Ocean. Journal of Physical Oceanography, 12(11), 1169-1188.

Mercier, H., Lherminier, P., Sarafanov, A., Gaillard, F., Daniault, N., Desbruyères, D., Falina, A., Ferron, B., Gourcuff, C., Huck, T., Thierry, V. (2015). Variability of the meridional overturning circulation at the Greenland – Portugal OVIDE section from 1993 to 2010. Progress in Oceanography, 132, 250–261. https://doi.org/10.1016/j.pocean.2013.11.001

Messias, M.J., Watson, A.J., Johannessen, T., Oliver, K.I.C., Olsson, K.A., Fogelqvist, E., Olafsson, J., Bacon, S., Balle, J., Bergman, N., Budéus, G., Danielsen, M., Gascard, J.C., Jeansson, E., Olafsdottir, S.R., Simonsen, K., Tanhua, T., Van Scoy, K., Ledwell, J.R. (2008). The Greenland Sea tracer experiment 1996–2002: Horizontal mixing and transport of Greenland Sea Intermediate Water. Progress in Oceanography, 78, 85–105. https://doi.org/10.1016/J.POCEAN.2007.06.005

Millero, F.J., Zhang, J., Lee, K., Campbell, D.M. (1993). Titration alkalinity of seawater. 44, 153–165.

Mintrop, L., Pérez, F.F., González-Dávila, M., Santana-Casiano, J.M., Körtzinger, A. (2000). Alkalinity determination by potentiometry: Intercalibration using three different methods. Ciencias Marinas, 26, 23–37. https://doi.org/10.7773/cm.v26i1.573

Moss, R. H., Edmonds, J. A., Hibbard, K. A., Manning, M. R., Rose, S. K., Van Vuuren, D. P., Carter, T. R., Emori, S., Kainuma, M., Kram, T., Meehl, G. A., Mitchell, J. F. B., Nakicenovic, N., Riahi, K., Smith, S. J., Stouffer, R. J., Thomson, A. M., Weyant, J. P., and Wilbanks, T. J. (2010). The next generation of scenarios for climate change research and assessment. *Nature*, *463*(7282), 747-756. https://doi.org/10.1038/nature08823

Mucci, A. (1983). The solubility of calcite and aragonite in seawater at various salinities, temperatures, and one atmosphere total pressure. American Journal of Science, 283(7), 780-799.

Olafsson, J., Olafsdottir, S.R., Benoit-Cattin, A., Danielsen, M., Arnarson, T.S., Takahashi, T. (2009). Rate of Iceland Sea acidification from time series measurements. Biogeosciences, 6, 2661–2668. https://doi.org/10.5194/bg-6-2661-2009

Olafsson, J., Olafsdottir, S.R., Benoit-Cattin, A., Takahashi, T. (2010). The Irminger Sea and the Iceland Sea time series measurements of seawater carbon and nutrient chemistry 1983-2008. Earth System Science Data, 2, 99–104. https://doi.org/10.5194/essd-2-99-2010

Orr, J.C., Epitalon, J.-M., Dickson, A. G., Gattuso, J.-P., (2018). Routine uncertainty propagation for the marine carbon dioxide system. Marine Chemistry 207, 84-107. https://doi.org/10.1016/j.marchem.2018.10.006

Orr, J.C., Fabry, V.J., Aumont, O., Bopp, L., Doney, S.C., Feely, R.A., Gnanadesikan, A., Gruber, N., Ishida, A., Joos, F., Key, R.M., Lindsay, K., Maier-Reimer, E., Matear, R., Monfray, P., Mouchet, A., Najjar, R.G., Plattner, G.K., Rodgers, K.B., Sabine, C.L., Sarmiento, J.L., Schlitzer, R., Slater, R.D., Totterdell, I.J., Weirig, M.F., Yamanaka, Y., Yool, A. (2005). Anthropogenic ocean acidification over the twenty-first century and its impact on calcifying organisms. Nature, 437, 681–686. [https://doi.org/10.1038/nature

Ostle C., P. Landschützer, M. Edwards, M. Johnson, S. Schmidtko, U. Schuster, A. J. Watson and C. Robinson, 2022. Multidecadal changes in biology influence the variability of the North Atlantic carbon sink. Environ. Res. Lett. 17, 114056, DOI : 10.1088/1748-9326/ac9ecf

Pérez, F.F., Fontela, M., García-Ibáñez, M.I., Mercier, H., Velo, A., Lherminier, P., Zunino, P., De La Paz, M., Alonso-Pérez, F., Guallart, E.F., Padin, X.A. (2018). Meridional overturning circulation conveys fast acidification to the deep Atlantic Ocean. Nature, 554, 515–518. https://doi.org/10.1038/nature25493

Pérez, F.F., Fraga, F. (1987). Association constant of fluoride and hydrogen ions in seawater. Marine Chemistry, 21, 161–168. https://doi.org/10.1016/0304-4203(87)90036-3

Pérez, F.F., Mercier, H., Vázquez-Rodríguez, M., Lherminier, P., Velo, A., Pardo, P.C., Rosón, G., Ríos, A.F. (2013). Atlantic Ocean CO2 uptake reduced by weakening of the meridional overturning circulation. Nature Geoscience, 6, 146–152. https://doi.org/10.1038/ngeo1680

Pérez, F.F., Olafsson, J., Ólafsdóttir, S.R., Fontela, M., Takahashi, T. (2021). Contrasting drivers and trends of ocean acidification in the subarctic Atlantic. Scientific Reports, 11, 1–16. https://doi.org/10.1038/s41598-021-93324-3

Pérez, F.F., Vázquez-Rodríguez, M., Louarn, E., Padín, X.A., Mercier, H., Ríos, A.F. (2008). Temporal variability of the anthropogenic CO2 storage in the Irminger Sea. Biogeosciences, 5, 1669–1679. https://doi.org/10.5194/bg-5-1669-2008

Pérez, F.F., Vázquez-Rodríguez, M., Mercier, H., Velo, A., Lherminier, P., Ríos, A.F. (2010). Trends of anthropogenic CO2 storage in North Atlantic water masses. Biogeosciences, 7, 1789–1807. https://doi.org/10.5194/bg-7-1789-2010

Perez, F. F., Becker, M., Goris, N., Gehlen, M., Lopez-Mozos, M., Tjiputra, J., Olsen, A., Müller, J. D., Huertas, I. E., Chau, T. T. T., Cainzos, V., Velo, A., Benard, G., Hauck, J., Gruber, N., Wanninkhof, R. (2024). An assessment of CO2 storage and sea-air fluxes for the Atlantic Ocean and Mediterranean Sea between 1985 and 2018. Global Biogeochemical Cycles, 38, e2023GB007862. https://doi.org/10.1029/2023GB007862

Pickart, R.S., Spall, M.A., Ribergaard, M.H., Moore, G.W.K., Milliff, R.F. (2003). Deep convection in the Irminger Sea forced by the Greenland tip jet. Nature, 424, 152–156. https://doi.org/10.1038/nature01729

Piron, A., Thierry, V., Mercier, H., Caniaux, G. (2017). Gyre-scale deep convection in the subpolar North Atlantic Ocean during winter 2014–2015. Geophysical Research Letters, 44, 1439–1447. https://doi.org/10.1002/2016GL071895

Pollard, R.T., Griffiths, M.J., Cunningham, S.A., Read, J.F., Pérez, F.F., Ríos, A.F. (1996). Vivaldi 1991 - A study of the formation, circulation, and ventilation of Eastern North Atlantic Central Water. Progress in Oceanography, 37, 167–172. https://doi.org/10.1016/S0079-6611(96)00008-0

Portner, H.O., Langenbuch, M., & Reipschläger, A. (2004). Biological Impact of Elevated Ocean CO2 Concentrations: Lessons from Animal Physiology and Earth History. Journal of Oceanography, 60, 705–718.

Pörtner, H. O., et al. (2019). IPCC Special Report on the Ocean and Cryosphere in a Changing Climate. Wiley IPCC Intergovernmental Panel on Climate Change.

Ramette, R.W., Culberson, C.H., and Bates, R.G. (1977). Acid-base properties of tris(hydroxymethyl) aminomethane (tris) buffers in seawater from 5 to 40°C. Analytical Chemistry 49, 867—870. https://doi.org/10.1021/ac50014a049

Raven, J., Caldeira, K., Elderfield, H., Hoegh-Guldberg, O., Liss, P., Riebesell, U., Shepherd, J., Turley, C., & Watson, A. (2005). Ocean acidification due to increasing. Coral Reefs, 12/05, 68.

Read, J.F. (2000). CONVEX-91: Water masses and circulation of the Northeast Atlantic subpolar gyre. Progress in Oceanography, 48, 461–510. https://doi.org/10.1016/S0079-6611(01)00011-8

Riebesell, U., Zondervan, I., Rost, B., Tortell, P.D., Zeebe, R.E., Morel, F.M.M. (2000). Reduced calcification of marine plankton in response to increased atmospheric CO2. Nature, 407, 364–366. https://doi.org/10.1038/35030078

Ríos, A.F., Resplandy, L., García-Ibáñez, M.I., Fajar, N.M., Velo, A., Padin, X.A., Wanninkhof, R., Steinfeldt, R., Rosón, G., Pérez, F.F., Morel, F.M.M. (2015). Decadal acidification in the water masses of the Atlantic Ocean. Proceedings of the National Academy of Sciences, U.S.A., 112, 9950–9955. https://doi.org/10.1073/pnas.1504613112

Roberts, J.M., Wheeler, A.J., Freiwald, A., Cairns, S. (2009). Cold-Water Corals: The Biology and Geology of Deep-Sea Coral Habitats. Cambridge University Press. https://doi.org/10.1017/CBO9780511581588.

Robson, J., Hodson, D., Hawkins, E., Sutton, R. (2014). Atlantic overturning in decline? Nature Geoscience, 7, 2–3. https://doi.org/10.1038/ngeo2050

Robson, J., Ortega, P., Sutton, R. (2016). A reversal of climatic trends in the North Atlantic since 2005. Nature Geoscience, 9, 513–517. https://doi.org/10.1038/ngeo2727

Rodgers, K.B., Key, R.M., Gnanadesikan, A., Sarmiento, J.L., Aumont, O., Bopp, L., Doney, S.C., Dunne, J.R., Glover, D.M., Ishida, A., Ishii, M., Jacobson, A.R., Monaco, C. Lo, Maier-Reimer, E., Mercier, H., Metzl, N., Pérez, F.F., Rios, A.F., Wanninkhof, R., Wetzel, P., Winn, C.D., Yamanaka, Y. (2009). Using altimetry to help explain patchy changes in hydrographic carbon measurements. Journal of Geophysical Research: Ocean, 114, 1–20. https://doi.org/10.1029/2008JC005183

Sabine, C.L., Feely, R.A., Gruber, N., Key, R.M., Lee, K., Bullister, J.L., Wanninkhof, R., Wong, C.S., Wallace, D.W.R., Tilbrook, B., Millero, F.J., Peng, T.H., Kozyr, A., Ono, T., Rios, A.F. (2004a). The oceanic sink for anthropogenic CO2. Science, 305, 367–371. https://doi.org/10.1126/science.1097403

Sabine, C.L., Feely, R.A., Gruber, N., Key, R.M., Lee, K., Bullister, J.L., Wanninkhof, R., Wong, C.S., Wallace, D.W.R., Tilbrook, B., Millero, F.J., Peng, T.H., Kozyr, A., Ono, T., Rios, A.F. (2004b). The oceanic sink for anthropogenic CO2. Science, 305, 367–371. https://doi.org/10.1126/SCIENCE.1097403/SUPPL_FILE/SABINE.SOM.PDF

Santana-Casiano, J. M., González-Dávila, M., and Curbelo-Hernández, D. (2023). Surface-to-bottom data of total alkalinity, total inorganic carbon, pH and dissolved oxygen in the subpolar North Atlantic along the CLIVAR 59.5N hydrographic section during 2009-2019. [Data set]. Zenodo. https://doi.org/10.5281/zenodo.10276222

Santana-Casiano, J.M., González-Dávila, M., Rueda, M.-J., Llinás, O., González-Dávila, E.-F. (2007). The interannual variability of oceanic CO2 parameters in the northeast Atlantic subtropical gyre at the ESTOC site. Global Biogeochemical Cycles, 21. https://doi.org/10.1029/2006GB002788

Sarafanov, A., Falina, A., Mercier, H., Sokov, A., Lherminier, P., Gourcuff, C., Gladyshev, S., Gaillard, F., and Daniault, N. (2012). Mean full-depth summer circulation and transports at the northern periphery of the Atlantic Ocean in the 2000s. Journal of Geophysical Research: Oceans, 117(C1).

Sarafanov, A., Falina, A., Sokov, A., Zapotylko, V., Gladyshev, S. (2018). Ship-Based Monitoring of the Northern North Atlantic Ocean by the Shirshov Institute of Oceanology. The Main Results. In: Velarde, M., Tarakanov, R., Marchenko, A. (eds) The Ocean in Motion. Springer Oceanography. Springer, Cham. https://doi.org/10.1007/978-3-319-71934-4_25

Sarafanov, A., Mercier, H., Falina, A., and Sokov, A. (2010). Cessation and partial reversal of deep water freshening in the northern North Atlantic: observation-based estimates and attribution. Tellus A: Dynamic Meteorology and Oceanography, 62:1, 80-90. https://doi.org/10.1111/j.1600-0870.2009.00418.x

Sarmiento, J.L., Orr, J.C., Siegenthaler, U. (1992). A perturbation simulation of CO2 uptake in an ocean general circulation model. Journal of Geophysical Research: Ocean, 97, 3621–3645. https://doi.org/10.1029/91JC02849

Saunders, P. M., (2001). Chapter 5.6 The dense northern overflows. Int. Geophys., 77, 401–417. https://doi.org/10.1016/S0074-6142(01)80131-5

Sauzède, R., Bittig, H.C., Claustre, H., de Fommervault, O.P., Gattuso, J.P., Legendre, L., Johnson, K.S. (2017). Estimates of water-column nutrient concentrations and carbonate system parameters in the global ocean: A novel approach based on neural networks. Frontiers in Marine Science, 4, 1–17. https://doi.org/10.3389/fmars.2017.00128

Schlitzer, R. (2021). Ocean Data View. Available at: https://odv.awi.de.

Schmitz Jr, W. J., & McCartney, M. S. (1993). On the north Atlantic circulation. Reviews of Geophysics, 31(1), 29-49.

Schott, F. A., & Brandt, P. (2007). Circulation and deep water export of the subpolar North Atlantic during the 1990's. Washington DC American Geophysical Union Geophysical Monograph Series, 173, 91-118.

Sharp, J.D., Pierrot, D., Humphreys, M.P., Epitalon, J.-M., Orr, J.C., Lewis, E.R., Wallace, D.W.R. (2023, Jan. 19). CO2SYSv3 for MATLAB (Version v3.2.1). Zenodo. http://doi.org/10.5281/zenodo.3950562

Smeed, D.A., Josey, S.A., Beaulieu, C., Johns, W.E., Moat, B.I., Frajka-Williams, E., Rayner, D., Meinen, C.S., Baringer, M.O., Bryden, H.L., McCarthy, G.D. (2018). The North Atlantic Ocean Is in a State of Reduced Overturning. Geophysical Research Letters, 45, 1527–1533. https://doi.org/10.1002/2017GL076350

Steinfeldt, R., Rhein, M., Bullister, J.L., Tanhua, T. (2009). Inventory changes in anthropogenic carbon from 1997 – 2003 in the Atlantic Ocean between 20 ° S and 65 ° N, 23, 1–11. https://doi.org/10.1029/2008GB003311

Stephens, T. (2021). Ocean Acidification. In: Research Handbook on Law, Governance and the Planetary Boundaries. 22, 295–308. https://doi.org/10.4337/9781789902747.00025

Stramma, L., Kieke, D., Rhein, M., Schott, F., Yashayaev, I., Koltermann, K.P. (2004). Deep water changes at the western boundary of the subpolar North Atlantic during 1996 to 2001. Deep Sea Research Part I: Oceanographic Research Papers, 51, 1033–1056. https://doi.org/10.1016/J.DSR.2004.04.001

Sutherland, D. A., and Pickart, R. S. (2008). The East Greenland coastal current: Structure, variability, and forcing. Progress in Oceanography, 78(1), 58-77.

Takahashi, T., Olafsson, J., Goddard, J.G., Chipman, D.W., Sutherland, S.C. (1993). Seasonal variation of CO2 and nutrients in the high-latitude surface oceans: A comparative study. Global Biogeochemical Cycles, 7, 843–878. https://doi.org/10.1029/93GB02263

Takahashi, T., Sutherland, S.C., Wanninkhof, R., Sweeney, C., Feely, R.A., Chipman, D.W., Hales, B., Friederich, G., Chavez, F., Sabine, C., Watson, A., Bakker, D.C.E., Schuster, U., Metzl, N., Yoshikawa-Inoue, H., Ishii, M., Midorikawa, T., Nojiri, Y., Körtzinger, A., Steinhoff, T., Hoppema, M., Olafsson, J., Arnarson, T.S., Tilbrook, B., Johannessen, T., Olsen, A., Bellerby, R., Wong, C.S., Delille, B., Bates, N.R., de Baar, H.J.W. (2009). Climatological mean and decadal change in surface ocean pCO2, and net sea-air CO2 flux over the global oceans. Deep Sea Research Part II: Topical Studies in Oceanography, 56, 554–577. https://doi.org/10.1016/j.dsr2.2008.12.009

Tanhua, T., Körtzinger, A., Friis, K., Waugh, D.W., Wallace, D.W.R. (2007). An estimate of anthropogenic CO2 inventory from decadal changes in oceanic carbon content. Proceedings of the National Academy of Sciences, U.S.A., 104, 3037–3042. https://doi.org/10.1073/pnas.0606574104

Tesdal, J.E., Abernathey, R.P., Goes, J.I., Gordon, A.L., Haine, T.W.N. (2018). Salinity trends within the upper layers of the subpolar North Atlantic. Journal of Climate, 31, 2675–2698. https://doi.org/10.1175/JCLI-D-17-0532.1

Thomas, H., Prowe, A.E.F., Lima, I.D., Doney, S.C., Wanninkhof, R., Greatbatch, R.J., Schuster, U., Corbière, A. (2008). Changes in the North Atlantic Oscillation influence CO2 uptake in the North Atlantic over the past 2 decades. Global Biogeochemical Cycles, 22, 1–13. https://doi.org/10.1029/2007GB003167

Tjiputra, J.F., Olsen, A., Bopp, L., Lenton, A., Pfeil, B., Roy, T., Segschneider, J., Totterdell, I., Heinze, C. (2014). Long-term surface pCO2 trends from observations and models. Tellus, Series B: Chemical and Physical Meteorology, 66, 1–24. https://doi.org/10.3402/tellusb.v66.23083

Touratier, F., Azouzi, L., Goyet, C. (2007). CFC-11, Δ14C and 3H tracers as a means to assess anthropogenic CO2 concentrations in the ocean. Tellus, Series B: Chemical and Physical Meteorology, 59, 318–325. https://doi.org/10.1111/j.1600-0889.2006.00247.x

Tsuchiya, M., Talley, L.D., McCartney, M.S. (1992). An eastern Atlantic section from Iceland southward across the equator. Deep Sea Research Part A: Oceanographic Research Papers, 39, 1885–1917. https://doi.org/10.1016/0198-0149(92)90004-D

Urban-Rich, J., Dagg, M., Peterson, J. (2001). Copepod grazing on phytoplankton in the Pacific sector of the Antarctic polar front. Deep Sea Research Part II: Topical Studies in Oceanography, 48, 4223–4246. https://doi.org/10.1016/S0967-0645(01)00087-X

Våge, K., Pickart, R.S., Thierry, V., Reverdin, G., Lee, C.M., Petrie, B., Agnew, T.A., Wong, A., Ribergaard, M.H. (2009). Surprising return of deep convection to the subpolar North Atlantic Ocean in winter 2007-2008. Nature Geoscience, 2, 67–72. https://doi.org/10.1038/ngeo382

Van Aken, H.M., and Becker, G. (1996). Hydrography and through-flow in the north-eastern North Atlantic Ocean: the NANSEN project. Prog. Oceanogr. 38, 297–346. https://doi.org/10.1016/S0079-6611(97)00005-0

Van Aken, H. M., and De Boer, C. J. (1995). On the synoptic hydrography of intermediate and deep water masses in the Iceland Basin. Deep Sea Research Part I: Oceanographic Research Papers, 42(2), 165-189.

Van Heuven, S., D. Pierrot, J.W.B. Rae, E. Lewis, and D.W.R. Wallace (2011). MATLAB Program Developed for CO2 System Calculations. ORNL/CDIAC-105b. Carbon Dioxide Information Analysis Center, Oak Ridge National Laboratory, U.S. Department of Energy, Oak Ridge, Tennessee. https://doi.org/10.3334/CDIAC/otg.CO2SYS_MATLAB_v1.1

Van Vuuren, D. P., Edmonds, J., Kainuma, M., Riahi, K., Thomson, A., Hibbard, K., Hurtt, G. C., Kram, T., Krey, V., Lamarque, J-F., Masui, T., Meinshausen, M., Nakicenovic, N., Smith, S. J., and Rose, S. K. (2011). The representative concentration pathways: an overview. *Climatic change*, *109*, 5-31. https://doi.org/10.1007/s10584-011-0148-z

Vázquez-Rodríguez, M., Padin, X.A., Pardo, P.C., Ríos, A.F., Pérez, F.F. (2012). The subsurface layer reference to calculate preformed alkalinity and air-sea CO2 disequilibrium in the Atlantic Ocean. J. Mar. Syst. 94, 52–63. https://doi.org/10.1016/j.jmarsys.2011.10.008

Vázquez-Rodríguez, M., Pérez, F.F., Velo, A., Ríos, A.F., Mercier, H. (2012). Observed acidification trends in North Atlantic water masses. Biogeosciences 9, 5217–5230. https://doi.org/10.5194/bg-9-5217-2012

Vázquez-Rodríguez, M., Touratier, F., Monaco, C. Lo, Waugh, D.W., Padin, X.A., Bellerby, R.G.J., Goyet, C., Metzl, N., Ríos, A.F., Pérez, F.F. (2009). Anthropogenic carbon distributions in the Atlantic Ocean: Data-based estimates from the Arctic to the Antarctic. Biogeosciences 6, 439–451. https://doi.org/10.5194/BG-6-439-2009

Wallace, D. W. (2001). Storage and transport of excess CO2 in the oceans: The JGOFS/WOCE global CO2 survey. In International Geophysics (Vol. 77, pp. 489-L). Academic Press. https://doi.org/10.1016/S0074-6142(01)80136-4

Watson, A.J., Schuster, U., Bakker, D.C.E., Bates, N.R., Corbière, A., González-Davila, M., Friedrich, T., Hauck, J., Heinze, C., Johannessen, T., Körtzinger, A., Metzl, N., Olafsson, J., Olsen, A., Oschlies, A., Antonio Padin, X., Pfeil, B., Magdalena Santana-Casiano, J., Steinhoff, T., Telszewski, M., Rios, A.F., Wallace, D.W.R., Wanninkhof, R. (2009). Tracking the variable North Atlantic sink for atmospheric CO2. Science (80-.). 326, 1391–1393. https://doi.org/10.1126/science.1177394

Winkler, L. W. (1888). Die bestimmung des im wasser gelösten sauerstoffes. Berichte der deutschen chemischen Gesellschaft, 21(2), 2843-2854.

Xu, X., Hurlburt, H.E., Jr, W.J.S., Zantopp, R., Fischer, J., Hogan, P.J. (2013). On the currents and transports connected with the atlantic meridional overturning circulation in the subpolar North Atlantic. J. Geophys. Res. 118, 502–516. https://doi.org/10.1002/jgrc.20065

Yashayaev, I. (2007). Hydrographic changes in the Labrador Sea, 1960–2005. Progress in Oceanography, 73(3-4), 242-276. https://doi.org/10.1016/j.pocean.2007.04.015

Yashayaev, I., Dickson, B. (2008). Transformation and Fate of Overflows in the Northern North Atlantic. In: Dickson, R.R., Meincke, J., Rhines, P. (eds) Arctic–Subarctic Ocean Fluxes. Springer, Dordrecht. https://doi.org/10.1007/978-1-4020-6774-7_22

Yashayaev, I., Holliday, N. P., Bersch, M., and van Aken, H. M. (2008). The history of the Labrador Sea Water: Production, spreading, transformation and loss. Arctic–Subarctic Ocean Fluxes: Defining the Role of the Northern Seas in Climate, 569-612.

Yashayaev, I., Lazier, J., & Clarke, R. (2003). Temperature and salinity in the central Labrador Sea during the 1990s and in the context of the longer-term change. Retrieved from https://doi.org/10.17895/ices.pub.19271729